

10-16-2015 12:00 AM

## Apodized-Aperture Pixel Design X-Ray Detector for Improvement of Detective Quantum Efficiency at High Spatial Frequencies

Elina Ismailova, *The University of Western Ontario*

Supervisor: Dr Ian Cunningham, *The University of Western Ontario*

A thesis submitted in partial fulfillment of the requirements for the Master of Science degree in Medical Biophysics

© Elina Ismailova 2015

Follow this and additional works at: <https://ir.lib.uwo.ca/etd>



Part of the [Medicine and Health Sciences Commons](#)

---

### Recommended Citation

Ismailova, Elina, "Apodized-Aperture Pixel Design X-Ray Detector for Improvement of Detective Quantum Efficiency at High Spatial Frequencies" (2015). *Electronic Thesis and Dissertation Repository*. 3320.  
<https://ir.lib.uwo.ca/etd/3320>

This Dissertation/Thesis is brought to you for free and open access by Scholarship@Western. It has been accepted for inclusion in Electronic Thesis and Dissertation Repository by an authorized administrator of Scholarship@Western. For more information, please contact [wlsadmin@uwo.ca](mailto:wlsadmin@uwo.ca).

**APODIZED-APERTURE PIXEL DESIGN X-RAY DETECTOR FOR  
IMPROVEMENT OF DETECTIVE QUANTUM EFFICIENCY AT HIGH SPATIAL  
FREQUENCIES**

by

**Elina Ismailova**

Graduate Program in Medical Biophysics

A thesis submitted in partial fulfillment  
of the requirements for the degree of  
**Master of Science**

The School of Graduate and Postdoctoral Studies  
The University of Western Ontario  
London, Ontario, Canada

© Elina Ismailova 2015

## Abstract

The detective quantum efficiency (DQE) is a characteristic of x-ray imaging systems describing how well a system can produce high signal-to-noise ratio images compared to an ideal detector. In medical radiography, increases in DQE result directly in increases in image SNR for a given x-ray exposure, and improved SNR has been shown to improve breast cancer detection rates in screening programs. Typically, modern x-ray detectors have DQE values about 0.6 to 0.7 at low spatial frequencies and 0.2 to 0.3 or less at high spatial frequencies. We describe a method to improve the high frequency DQE by developing a novel apodized-aperture pixel (AAP) design that can be implemented with detectors having very small elements. We show theoretically that the high-frequency DQE can be doubled using this approach. Experimental validation shows an increase from 0.2 to 0.4 at the sampling cut-off frequency (2.5 cycles/mm) for a laboratory CMOS/CsI detector. It is predicted the high-frequency DQE of a Se-based detector for mammography could be increased from 0.35 to 0.7. Such increases would improve visualization of small objects and fine detail in x-ray imaging by a factor of two.

## Keywords

DQE optimization, x-ray detector, aliasing reduction

## Acknowledgments

I am very grateful to my supervisor, Dr Cunningham for guidance and helpful discussions on the project. I would like to acknowledge CIHR and NSERC sources of funding for the research opportunity at Robarts Research Institute. Many thanks to my Russian family for their love and to my Canadian friends for support.

# Table of Contents

Abstract .....	ii
Keywords .....	ii
Acknowledgments .....	iii
Table of Contents .....	iv
List of Figures .....	vi
List of Abbreviations .....	ix
Chapter 1 .....	1
1 Introduction .....	1
1.1 Basic Technology of Digital Radiography Detectors .....	2
1.2 Common modern technologies .....	3
1.2.1 Photostimulable storage phosphor detectors .....	3
1.2.2 Scintillator with charge coupled device systems .....	3
1.2.3 Active-matrix flat panel image detectors .....	4
1.2.4 Complimentary metal-oxide semiconductor detectors .....	6
1.3 Background on DQE and why it is important .....	6
1.4 Cascaded system analysis to model DQE .....	9
1.4.1 Quantum Gain .....	10
1.4.2 Quantum Selection .....	11
1.4.3 Collecting quanta in detector elements .....	12
1.4.4 Evaluating signal at discrete positions and noise aliasing .....	13
1.5 DQE improvement addressed in previous works .....	17
1.6 Description of proposed solution (AAP) .....	22
1.7 Brief overview of the thesis .....	22
1.8 References .....	23

Chapter 2.....	28
2 AAP detector design .....	28
2.1 Introduction.....	28
2.2 Methods.....	30
2.2.1 Conventional Detector Design.....	30
2.2.2 Apodized Aperture Pixel (AAP) design .....	34
2.3 Results.....	37
2.4 Conclusions.....	39
2.5 References.....	40
Chapter 3.....	41
3 Optimization.....	41
3.1 Methods.....	42
3.2 Results.....	43
3.3 Conclusions.....	44
Chapter 4.....	46
4 Overview and Conclusions .....	46
4.1 Limitations .....	46
4.2 Conclusions.....	46
4.3 Future work.....	48
4.4 References.....	48
Appendix A: Copyright approval.....	49
Curriculum Vitae .....	50

## List of Figures

Figure 1-1. Illustration of x-ray interaction and charge collection for “indirect” (A) and “direct” (B) x-ray detectors.....	5
Figure 1-2. Representative image from a system with high DQE (purple) and simulated low DQE (green) illustrating the impact of DQE on image quality. ....	6
Figure 1-3. Image quality vs exposure for 0.16 uR, 45 q/mm <sup>2</sup> (fluoroscopy); 16 uR, 4500 q/mm <sup>2</sup> (radiography) and 24 uR, 6700 q/mm <sup>2</sup> (radiography). ....	7
Figure 1-4. Illustration of quantum gain in 1-D, characterized by gain mean and variance. Every point (quantum) in the input is replaced with $g$ secondary quanta in the output at the same location. Bold vectors represent overlapping delta functions.....	11
Figure 1-5. Summation of secondary quanta, represented as a convolution with a rectangle function in the spatial domain with a width equal to that of detector elements, $a$ . ....	13
Figure 1-6. Signal evaluation from discrete detector elements is represented by multiplication with a set of delta-functions, resulting in $d$ . The superscript dagger is used to indicate a discrete signal represented as a sequence of scaled delta functions.....	14
Figure 1-7. Sampling a function at uniform spacings $x_0$ causes spectral aliasing of the presampling signal if it contains frequency components above the sampling cut-off frequency $u=1/x_0$ . We denote Wiener NPS as $W(u)$ on CSA illustrations. ....	16
Figure 2-1. Schematic illustration of a conventional detector, consisting of a conversion layer where interacting x-ray quanta are converted to secondary quanta, such as light from a scintillator or liberated charges from a photoconductor, and a sensor array to collect secondary quanta. The sensor array consists of a two-dimensional array of elements having dimension $a$ . The corresponding cascaded model consists of: 0) spatial distribution of incident x-ray quanta $q_x(x)$ ; 1) conversion to secondary quanta $q_x(x)$ ; 2) integration of secondary quanta in sensor elements giving detector presampling signal	

$\mathbf{d}(\mathbf{x})$ ; 3) sampling at centers of elements giving a sequence of Dirac  $\delta$ -functions scaled by detectors output signals,  $\mathbf{d}^+(\mathbf{x})$ ..... 29

Figure 2-2. Illustration of signal and noise transfer through a conventional detector in spatial and spatial-frequency domains. Conversion to secondary quanta in step 1 has been omitted for brevity. The input,  $\mathbf{q}_x\mathbf{x} = \delta(\mathbf{x} - \mathbf{x}_i)$ , is a random distribution of x-ray quanta incident on the detector input, represented as a distribution of Dirac  $\delta$ -functions. The output is  $\mathbf{d}_a\mathbf{x}$ , **a set of regularly – spaced**  $\delta$ -functions on spacing  $a$ , scaled by the corresponding image pixel values..... 31

Figure 2-3. Schematic illustration of an apodized-aperture pixel structure. It differs from the conventional detector by using very small sensor elements of dimension  $\epsilon$  and filter  $f(\mathbf{x})$  to synthesize the detector presampling signal  $\mathbf{df}(\mathbf{x})$ . The sinc-shaped filter prevents noise aliasing while preserving the superior frequency response of the small elements, resulting in improved DQE..... 33

Figure 2-4. Illustration of signal and noise transfer through the apodized-aperture pixel design in spatial and spatial frequency domains. Step 1, conversion to secondary quanta in the converter, has been omitted for brevity. The output  $\mathbf{d}^+_A(\mathbf{x})$  is similar to that of the conventional detector except pixel values are synthesized from detector element signals as a convolution with  $f(\mathbf{x})$  at step 4). By choosing  $f(\mathbf{x}) = \text{sinc}(a\mathbf{u})$ , the effect of noise aliasing on the DQE is greatly reduced as illustrated here. .... 35

Figure 2-5. Comparison of conventional and apodized DQE as determined for ideal x-ray converter using the CSA model with physical elements of width  $\epsilon = 0.05$  mm and image pixels of width  $a = 0.2$  mm. The DQE is almost independent of spatial frequency and is doubled at the sampling cut-off frequency. .... 36

Figure 2-6. Experimental validation of the AAP concept using a CMOS/CsI-based detector (Xmaru, Rayence Co.) with physical sensor elements of 0.05 mm (RQA-5 spectrum, 0.66 mR detector exposure). Left: Presampling MTF and DQE obtained using images constructed by 4x4 binning of detector data to simulate a conventional detector with 0.2-mm elements. Right: Presampling MTF and DQE obtained using images



synthesized using the AAP approach to create 0.2-mm pixels. The MTF is increased at frequencies above 1.5 cycles/mm and all frequencies above 2.5 cycles/mm are removed from the image. The high-frequency DQE is increased from 0.2 to 0.4. Blue curves – experimental data, red points – estimates at spacing 0.25 cy/mm. ....	38
Figure 3-1. Illustration of the shrinking mechanism of the AAP approach. ....	43
Figure 3-2. Illustration of the expanding algorithm of AAP detector design. ....	44
Figure 3-3. MatLab simulation of an AAP filter optimization. Left plot: evaluation of the DQE area as an optimization criterion that determines the AAP filter aperture (right plot). ....	45

## List of Abbreviations

1-D	One-dimensional
2-D	Two-dimensional
AMFPI	Active-matrix flat-panel imaging
CSA	Cascaded system analysis
CSF	Characteristic spread function
CTF	Characteristic transfer function
DQE	Detective quantum efficiency
ESF	Edge-spread function
FT	Fourier transform
IRF	Impulse-response function
LSI	Linear and shift invariant
MTF	Modulation-transfer function
NPS	Noise-power spectrum
PDF	Probability-density function
PSF	Point-spread function
SNR	Signal-to-noise ratio
WSCS	Wide-sense cyclostationary
WSS	Wide-sense stationary

# Chapter 1

## 1 Introduction

Radiographic images are formed by the transmission of x rays (electromagnetic radiation in the energy range of approximately 20 eV – 120 keV) through patients, and radiography is the most widely used medical-imaging procedure with over 20 million diagnostic x-ray procedures performed each year in Canada [1] [2]. Image contrast results from differences in x-ray transmission through different tissues. Since x-ray interactions and detection are random processes, there is a statistical uncertainty in the number of x-ray quanta that interact in the imaging detector. This results in image “noise” that reduces image quality and can obscure visualization of small or low-contrast structures. Image quality can normally be improved by using higher radiation exposures. However, radiation exposure to patients is associated with a risk of developing radiation-induced cancers, cataracts, and other consequences [2]. About one case out of 2000 cancer cases is associated with diagnostic radiation [3]. The linear hypothesis [4] is normally adopted in which we assume there is no threshold for cancer risk, even at low exposures, and risk is proportional to dose. It is therefore important that x-ray imaging systems be designed to produce images with adequate quality for the medical task while minimizing patient exposure.

The ability of an x-ray system to produce high-quality images is described by the system’s detective quantum efficiency (DQE). The DQE describes image SNR relative to that of an ideal (photon-counting) detector for a specified detector exposure. It is expressed as a function of spatial frequency (cycles/mm) where low frequencies correspond to the visualization of large image structures and high frequencies describe visualization of small structures and fine image detail. An improved DQE will improve image SNR. The DQE of modern imaging systems can be relatively good (close to unity) at low spatial frequencies, but generally decreases substantially with increasing frequency. There are several reasons for this decrease. My goal in this thesis is to develop a novel x-ray detector design to achieve improved high-frequency DQE by reducing noise aliasing.

## 1.1 Basic Technology of Digital Radiography Detectors

Digital radiography is a form of x-ray imaging, in which traditional photographic films are replaced with digital x-ray sensors and digital image capture devices. These improvements over film-screen systems permitted immediate image preview and the possibility of image processing [5]. In addition, some studies have shown that less radiation exposure is required for creating digital images in contrast to film radiographs by up to 70 % [6]. Many modern radiography departments now rely exclusively on digital technologies.

The first digital radiographs for medical applications were obtained in the 1980s [7]. They implemented optical-lens assemblies to focus x-ray-generated light quanta from an x-ray phosphor (generally  $\text{Gd}_2\text{O}_2\text{S}$  based) onto a small-area charge-coupled device (CCD) photodetector [8]. In the late 1990s, active-matrix flat panel imaging (AMFPI) systems appeared, making use of x-ray to light converters (generally  $\text{Gd}_2\text{O}_2\text{S}$  or  $\text{CsI}$  based) with large-area photodiode arrays converting incident x-ray quanta into an image signal. Both CCD and flat-panel detectors use active readout of detector data to generate a digital image.

Flat panel detectors (FPD) are subdivided as direct (photoconductor based) and indirect (scintillator based) types depending on how x-ray energy is converted to a measureable signal. Indirect FPDs (Fig. 1.1 A) use a scintillator converter layer (generally  $\text{CsI}$  or  $\text{Gd}_2\text{O}_2\text{S}$ ) to convert interacting x-ray quanta into emitted light that is coupled to a photo-sensor array generally made from amorphous silicon (a-Si) thin-film transistors (TFT). The output signals from all detector elements are converted into digital values (proportional to absorbed x-ray energy) that can be displayed as a digital image. Direct FPDs (Fig. 1.1 B) differ because x-rays are used to liberate charges directly in the converter layer (generally amorphous selenium, a-Se) between layered electrodes and a TFT array is used to measure the liberated charge collected by high-voltage bias electrodes in each detector element. Direct detectors can have superior spatial resolution because optical scatter of quanta in the converter layer blurs the image more than charge migration in the photo-conductor converter layer [7].

## 1.2 Common modern technologies

A brief summary of detectors often found in modern x-ray imaging facilities is presented here.

### 1.2.1 Photostimulable storage phosphor detectors

This type of detector uses cassette-based storage phosphors that retain absorbed x-ray energy as a two-dimensional distribution of electrons trapped in semistable energy wells [9, 10]. A scanning laser beam activates trapped electrons to liberate luminescence quanta of a different wavelength. A photomultiplier system reads out the luminescence light as the phosphor is scanned to create a digital image, followed by a clearing of any residual signal to prepare for the next exposure. Cassette reading requires individual loading of cassettes in small batches in a reader by staff, which increases the cost as each cassette reading may take several minutes. Recent technological developments of storage phosphor detectors include development of components with low intrinsic lag for shorter read-out time, “dual-side” phosphor deposition on a transparent material for improvement of x-ray detection efficiency, improved stimulated luminescence efficiency for higher SNR, and structured PSP materials such as CsBr that allow improved spatial resolution and detection efficiency. Cassette-based CR detectors are used for digital mammography with special adjustments to read-out electronics and laser beam. The zero-frequency DQE values of CR systems are typically 0.3 to 0.45 [10, 11]

### 1.2.2 Scintillator with charge coupled device systems

Charge-coupled device (CCD) systems consist of a scintillator converter that converts absorbed x-ray energy into light quanta which are then focussed on to a small-area CCD [12]. The CCD typically has very low readout noise, but the number of optical quanta per interacting x-ray photon focussed onto the CCD may not be large enough to prevent a secondary quantum sink, resulting in reduced image SNR and DQE [13].

One potential reason for low light collection is the wide angle of light emission from most scintillators. A non-structured phosphor, such as  $\text{Gd}_2\text{O}_2\text{S}$ , has high light dispersion properties and, therefore, only a small fraction of light can be focused onto the CCD [14].

A structured phosphor, such as CsI, generates more focused light output, and thus higher light collection efficiency and potentially higher SNR of output image for a given incident x-ray exposure. However, direct x-ray exposure of the CCD can introduce noise and device deterioration, requiring a relatively large enclosure to locate the CCD out of direct x-ray beam exposure and mirror optics to reflect light to the CCD. CCD imaging systems based on slot scan image acquisition demonstrated very good clinical results for chest and whole body imaging [15] [16].

### 1.2.3 Active-matrix flat panel image detectors

AMFPI technologies are based on thin-film transistor (TFT) arrays created using amorphous silicon (a-Si) with lithographic etching [17, 18]. They consist of a matrix of detector elements arranged with a centre-to-centre spacing of 100 – 200  $\mu\text{m}$  [19]. Components of each AMFPI detector include a thin-film transistor, a charge collection electrode and a storage capacitor. After exposure to x-rays, the active matrix array is read out, one row at a time, by activating gate lines that turn on the corresponding thin-film transistors and allows stored charges to reach the amplifier. The measured charge is converted to a proportional voltage and digitized to create a digital image matrix. Detector readout time is determined by the relatively low-performance of TFT electronics and the number of amplifiers used. Sensitivity is influenced by the detector element fill factor, describing the fraction of each element that is sensitive to secondary quanta relative to the centre-to-centre spacings of the elements. The ideal case of 100% fill factor corresponds to the most efficient collection of x-ray information. Collection efficiency is degraded by electronic components and connection lines of the TFT. These detectors often have faulty or disfunctional detector elements caused by malfunctioning detector elements or electronics gates. The damaged response is corrected by interpolation to the nearby detector elements filling expected information.

AMFPI detectors are divided into “indirect” and “direct” x-ray systems as illustrated in Fig. 1-1 [17]. Indirect systems use a-Si TFT technology to create a photodiode array to measure light emitted from a phosphor converter material. Each light photon liberates a charge carrier that is collected in a capacitor in each detector element. Both  $\text{Gd}_2\text{O}_2\text{S}$  and structured CsI converters are widely used, but CsI has superior x-ray detection efficiency

and light production properties, and good spatial resolution [20]. Indirect systems use TFT technology to measure charges liberated directly by x-ray interactions in a photoconductor converter, generally amorphous selenium. Charges are collected by electric fields created by a bias voltage to prevent recombination and charge spreading in the a-Se layer [21]. The fill factor can be close to unity as electrode design can funnel charges along electric field lines. At present, indirect AMFPIs have shown good performance in conventional radiography applications and high-speed (dynamic) applications such as fluoroscopy due to high speed of image acquisition and read-out. Direct AMFPIs have wide implementation in digital mammography due to their higher spatial resolution properties [22].

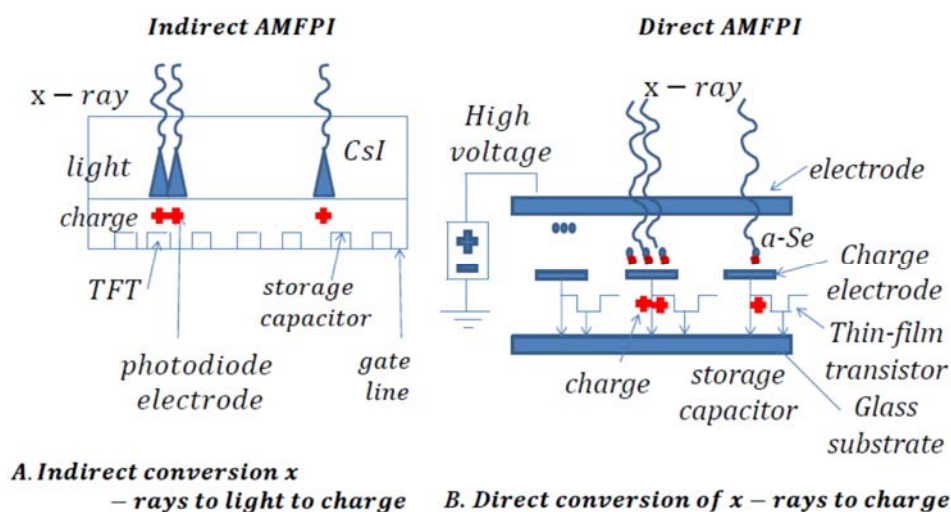


**Figure 1-1. Illustration of x-ray interaction and charge collection for “indirect” (A) and “direct” (B) x-ray detectors.**

The term DR (digital radiography) is often used to describe both direct and indirect systems, in contrast with CR systems. DR detectors can achieve DQE values of 0.5 to 0.7 at zero spatial frequency in modern imaging systems. This is generally superior to CR systems which implies that superior image quality (in terms of image SNR) can be achieved for the same patient exposures.

### 1.2.4 Complimentary metal-oxide semiconductor detectors

Complimentary metal-oxide semiconductor (CMOS) detectors are based on crystalline silicon matrix with built-in photodiodes, storage capacitors and active electronics operating at low voltage for image acquisition and readout processes [23]. CMOS can be used to create extremely high performance circuits for use in both direct and indirect detector designs. They have extremely low electronic noise, very fast readout performance, and can be used to create extremely small detector elements ( $\sim 25 \mu\text{m}$ ) in comparison to TFT arrays. However, until recently it has not been possible to manufacture large area CMOS arrays. In the past few years, prototype CMOS systems have been available with dimensions of 12 x 15 cm, and can be assembled together (typically on three sides only) to create larger arrays. While not available for general radiographic applications, CMOS-based systems have been used in special prototype applications [24], [25].

## 1.3 Background on DQE and why it is important

The detective quantum efficiency (DQE) is a metric describing image quality in terms of SNR relative to that obtained by an ideal (photon-counting) x-ray detector (Fig. 1-2).

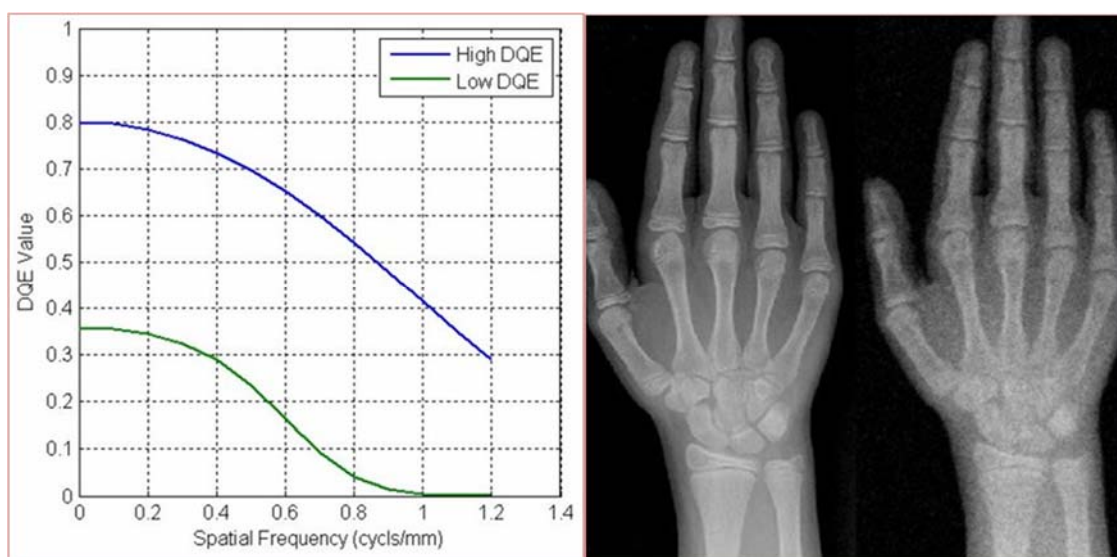


**Figure 1-2. Representative image from a system with high DQE (purple) and simulated low DQE (green) illustrating the impact of DQE on image quality.**



The importance of image SNR was highlighted recently in a study [26] that showed superior breast cancer detection rates improvement with DR compared to CR (34%, corresponding to 25% patient dose increase) in a screening mammography program in Ontario (Ontario Breast Screening Program, OBSP). They attributed the difference to the superior image SNR. As a result of this finding, CR systems are no longer accepted by the OBSP for mammography screening. Similar decisions have been made elsewhere. The implication is that further improvements in image SNR, resulting from improved DQE values, will further improve cancer detection rates in screening programs, and improve image quality in general in all of radiography.

Defined as the ratio of the squared image SNR to the number of incident x-ray photons, the DQE describes how efficiently a system preserves the Poisson statistics associated with incident x-ray photons to produce a high SNR image [27] (Fig. 1-3).

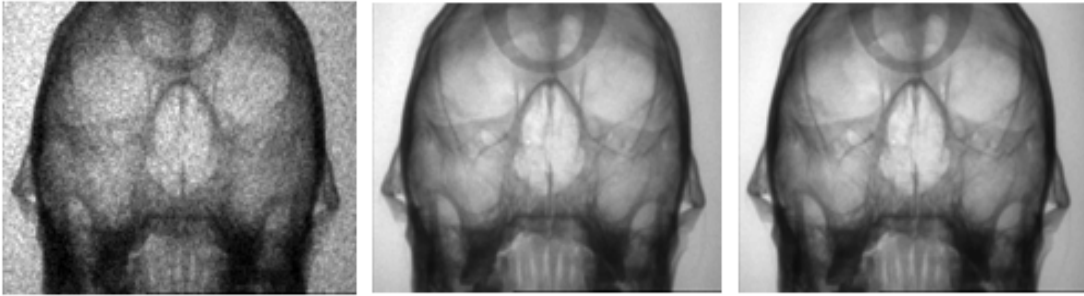


**Figure 1-3. Image quality vs exposure for 0.16 uR, 45 q/mm<sup>2</sup> (fluoroscopy); 16 uR, 4500 q/mm<sup>2</sup> (radiography) and 24 uR, 6700 q/mm<sup>2</sup> (radiography).**

The DQE can be evaluated as:

$$DQE(u) = \frac{\bar{d}^2 MTF^2(u)}{\bar{q} NPS(u)} \quad (1.1)$$

where  $q$  describes a distribution of incident x-ray quanta [quanta/mm<sup>2</sup>],  $d$  is the corresponding detector average digital output signal (assuming a linear detector),  $MTF(u)$  is the system modulation transfer function (MTF) describing spatial resolution as a function of spatial frequency  $u$  (Fourier conjugate of spatial coordinate  $x$ ), and  $NPS(u)$  is the Wiener noise power spectrum describing image noise.

High DQE values indicate less radiation is required to obtain a certain image quality. Similarly, increased DQE at the same radiation exposure leads to improved image quality. High DQE values at low spatial frequencies indicate high SNR for visualizing large image structures. High DQE at high spatial frequencies indicate high SNR for visualizing small structures and fine details. An ideal detector would have a DQE equal to 1 at any spatial frequency, resulting in an image SNR equal to that of the Poisson-distributed incident x-ray photons. In practice, many factors can degrade image SNR and therefore the DQE, particularly at high spatial frequencies. DQE was initially introduced as a measure of system performance to the medical imaging community by Shaw and Wagner [28] [29]. The effect of DQE on image quality is illustrated in Fig. 1-2. The left side illustrates an image from a system with a good DQE (purple curve). The right side illustrates the same image degraded (by blurring and adding noise) to correspond to the poor DQE (green curve). The difference between these systems is greatest at high spatial frequencies, resulting in very poor visualization of fine details in the right-hand image.

The DQE is closely related to a measure of image SNR called the noise-equivalent number of quanta (NEQ). The NEQ describes measured image SNR in terms of a number of Poisson-distributed incident x-ray quanta (per unit area) required by an ideal imaging system to give the same SNR. This gives an absolute scale on which to specify image SNR [28]. The NEQ is given by:

$$NEQ(\bar{q}, u) = \frac{|\bar{q}T(u)|^2}{NPS(u)} \quad (1.2)$$

An ideal imaging system will produce images with  $SNR^2 = NEQ = q$ .

Spatial resolution of a linear and shift-invariant (LSI) imaging system is described by the modulation transfer function (MTF), understood by considering an impulse input impulse described by delta-function  $\delta(x-x_0)$  located at  $x_0$ . For a system described by the operator  $S[ ]$ , the corresponding output  $d(x)$  will be  $S[\delta(x-x_0)]$  determined with the convolution integral of impulse response function with eigenvalues of the operator  $S$ :

$$d(x) = \int irf(x')e^{i2\pi u(x-x')}dx' = e^{i2\pi ux} \int irf(x')e^{-i2\pi ux'}dx' \quad (1.3)$$

where  $irf(x)$  is the impulse response function (IRF) of the system. The last integral is the Fourier transform of  $irf(x)$ , which we denote as the system characteristic function  $T(u)$ :

$$T(u) = \mathcal{F}irf(x) \quad (1.4)$$

which is equal to the system input scaled by the frequency-dependent factor  $T(u)$ . Modulation transfer function, MTF is given by the ration of the absolute value of the characteristic function and its zero-frequency value:

$$MTF(u) = \frac{|T(u)|}{T(0)} \quad (1.5)$$

and, by definition, has unity value at zero frequency. The MTF does not describe an imaging system as completely as the characteristic function  $T(u)$  because phase and scaling information are removed. Due to the magnitude operator, the MTF is a real-only function [30].

Fourier methods can be used to describe image noise, but only for LSI systems with wide-sense stationary (WSS) random noise processes, meaning the expected value (mean) and autocorrelation function are invariant to a shift in  $x$  (the image plane). Noise is then described by the Wiener noise power spectrum, equal to the Fourier transform of the autocovariance function, describing the spectral decomposition of noise variance [30]. Thus:

$$DQE(\bar{q}, u) = \frac{\bar{q}^2 \bar{G} MTF^2(u)}{NPS(u)} = \frac{\bar{d}^2 MTF^2(u)}{\bar{q} NPS(u)} \quad (1.6)$$

where  $G$  is a gain factor relating  $\bar{d}$  to  $\bar{q}$ .

## 1.4 Cascaded system analysis to model DQE

The relationship between the design of an x-ray system and its DQE can be determined using a “cascaded systems analysis” in which a system is represented as a cascade of operators that describe simple physical processes. Relationships describing transfer of signal and noise through each process are known, and can be cascaded to predict the overall

signal and noise performance (DQE) of an imaging system. Cascaded systems analysis (CSA) is based on linear systems theory developed in electrical engineering and communications theory and adapted to describe quantum-based imaging systems [31]. This approach was initiated by Rabbani, Shaw and Van Metter [32-34] who introduced the idea of a quantum-based amplification stage to describe conversion of x-ray quanta into light quanta to study signal and noise transfer in film-screen systems. It is assumed systems are mean-linear (meaning the mean system output is proportional to the mean input) and shift invariant. The CSA approach was generalized to include other physical processes including multiple parallel cascades by Yao and Cunningham [35] and spatiotemporal processes including lag [36] for more comprehensive models of DQE of x-ray imaging systems [37]. It is used in this project to predict the DQE improvement that will be achieved with the apodized-aperture pixel (AAP) structure.

The input to our CSA model is a spatial distribution of quanta described as a superposition of delta-functions with coordinates corresponding to quantum locations:

$$\tilde{q}(x) = \sum_{i=1}^{\tilde{N}} \delta(x - \tilde{x}_i) \quad (1.7)$$

where  $\tilde{x}_i$  is a random variable specifying location of the  $i$ th quantum and  $\tilde{N}$  is a random variable equal to the total number of quanta. Output of a digital imaging system is a matrix of digital values that characterize an image, proportional to the x-ray energy deposited in each detector element. The relationship between input x-ray quanta and output image data is represented as a serial cascade of elementary physical processes in the CSA model.

In the following subsections, elementary processes used in this work, and their signal and noise transfer characteristics, are described.

#### 1.4.1 Quantum Gain

Quantum gain is a process in which each input quantum (x-ray photon) is replaced by a random number of secondary quanta at the same location [38] as illustrated in Fig. 1-2. Examples include the conversion of interacting x-ray photons to a random number of

secondary quanta (light photons in a phosphor or liberated charge carriers in a photoconductor). The process is defined in terms of random variable  $\tilde{g}$  (gain) with a specified mean  $\bar{g}$  and variance  $\sigma_g^2$ . Multiple quanta will normally overlap in the output distribution when  $g > 0$ . Relationships describing output distribution of quanta, mean, modulation transfer function and Wiener noise power spectrum between input and output are given by:

$$\tilde{q}_{out}(x) = \tilde{g} \tilde{q}_{in}(x) \quad (1.8)$$

$$\bar{q}_{out} = \bar{g} \bar{q}_{in} \quad (1.9)$$

$$\bar{Q}_{out}(u) = \bar{g} \bar{Q}_{in}(u) \quad (1.10)$$

where  $Q(u)$  is the Fourier transform of  $q(x)$ , and

$$NPS_{out}(u) = \bar{g}^2 NPS_{in}(u) + \sigma_g^2 \bar{q}_{in} \quad (1.11)$$

#### 1.4.2 Quantum Selection

A special case of quantum gain is the random selection of quanta from a distribution of incident quanta (a quantum gain state where the gain sample value can be 1 or 0 only).

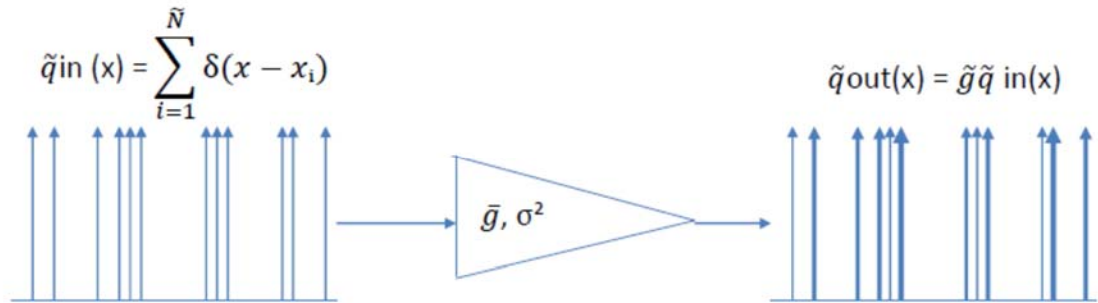


**Figure 1-4. Illustration of quantum gain in 1-D, characterized by gain mean and variance. Every point (quantum) in the input is replaced with  $g$  secondary quanta**

**in the output at the same location. Bold vectors represent overlapping delta functions.**

### 1.4.3 Collecting quanta in detector elements

The process of collecting secondary quanta in detector elements and producing an output signal proportional to the number collected is represented by this operation. The input is a spatial distribution of quanta (points), while the output is the signal from a detector element with size  $a$  located at position  $x$  for all  $x$ , giving:

$$\tilde{d}_{out}(x) = k \tilde{q}_{in}(x) * \Pi\left(\frac{x}{a}\right) \quad (1.12)$$

$$\bar{d}_{out} = k a \bar{q}_{in} \quad (1.13)$$

$$T_{out}(u) = \text{sinc}(au)T_{in}(u) \quad (1.14)$$

$$NPS_{out}(u) = k^2 a NPS_{in}(u) |\text{sinc}(au)|^2 \quad (1.15)$$

Here  $k$  is a scaling factor and  $\Pi(x/a)$  is a rectangle of width  $a$  and unity height. The function  $\text{sinc}(au)$  is called the “aperture MTF”. The aperture MTF describes how spatial frequencies are passed through detector elements. When quanta are integrated in elements of width  $a$ , the aperture MTF could be evaluated in terms of the characteristic function  $T_a$ , where  $a$  is the size of a detector element:

$$MTF_a(u) = \frac{|T_a(u)|}{T_a(0)} = |\text{sinc}(\pi au)| \quad (1.16)$$

If the size of a detector element decreases, the passband of the aperture MTF increases.

The output  $d_{out}(x)$  is a continuous function of  $x$ , and is sometimes called the detector “presampling” signal. It has physical meaning only at the positions of  $x$  corresponding to the centers of physical detector elements.

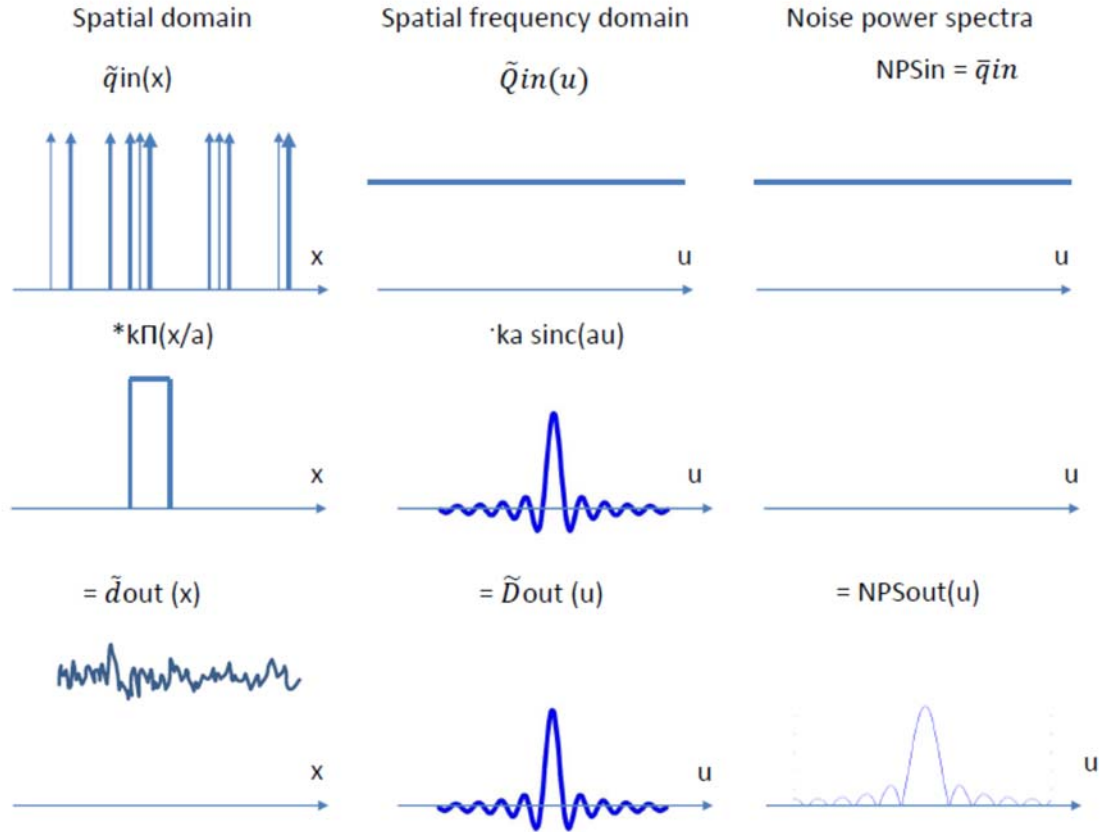


**Figure 1-5. Summation of secondary quanta, represented as a convolution with a rectangle function in the spatial domain with a width equal to that of detector elements,  $a$ .**

#### 1.4.4 Evaluating signal at discrete positions and noise aliasing

The process of evaluating sample values of a function at uniform spacings  $x_o$  is described by formulas 1.17 – 1.20, where superscript  $\dagger$  indicates a scaled delta function representing a discrete value and  $d^\dagger(x)$  describes the detector output signal as a series of uniformly spaced scaled delta functions:

$$\tilde{d}_{out}^+(x) = \bar{d}(x) \sum \delta(x - ix_o) \quad (1.17)$$

$$\bar{d}^+ = \bar{d}/x_o \quad (1.18)$$

$$T_{out}(u) = T_{in}(u) + \sum T_{in}(u \pm \frac{i}{x_o}) \quad (1.19)$$

$$W^+(u) = 1/\varepsilon^2 [W_\varepsilon(u) + W_\varepsilon(u \pm n/\varepsilon)] \quad (1.20)$$

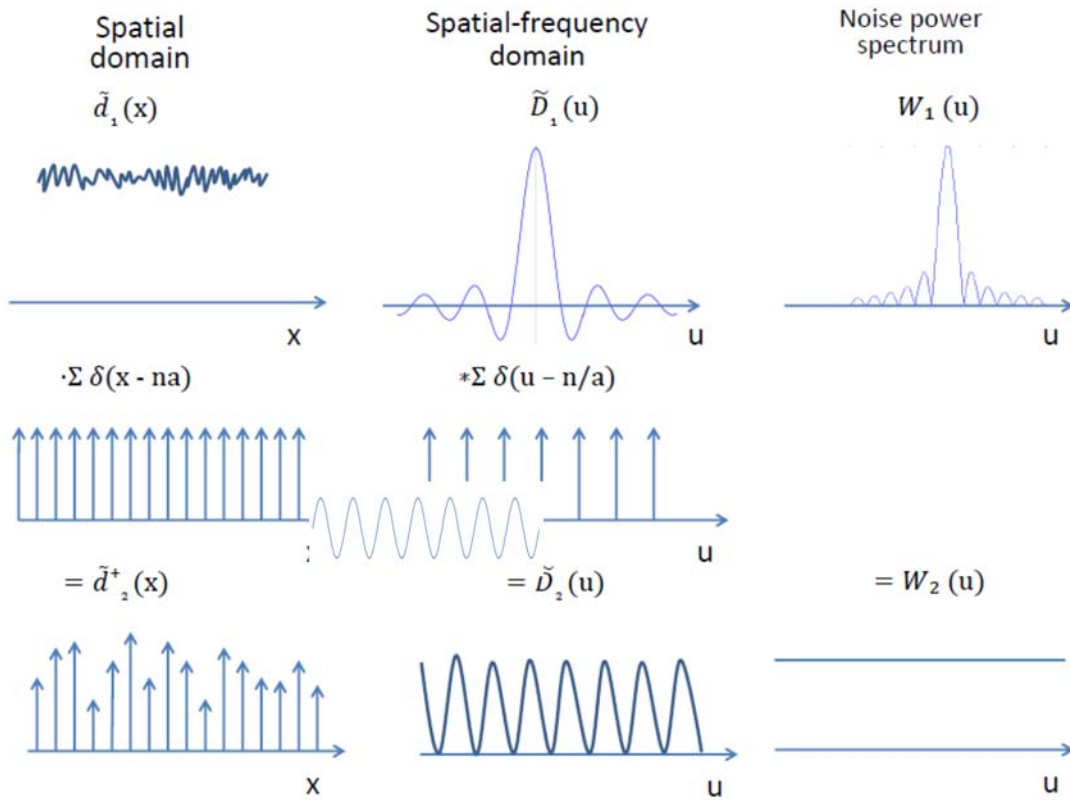


**Figure 1-6. Signal evaluation from discrete detector elements is represented by multiplication with a set of delta-functions, resulting in  $\bar{d}$ . The superscript dagger is used to indicate a discrete signal represented as a sequence of scaled delta functions.**

The maximum spatial frequency that can be represented by discrete samples on uniform spacings  $x_o$  is given by the Nyquist sampling cut-off frequency as  $U_{Nq} = 1/2x_o$ . The frequency components exceeding  $U_{Nq}$  are subjected to sampling in the output image, which



leads to folding of these components back into a region below  $U_{Nq}$ . This phenomenon is called aliasing. Noise components folded back below  $U_{Nq}$  are considered as noise aliasing that can degrade low-contrast detectability [39]. Noise is stochastic variation in image signal. System noise can be evaluated in terms of variance in measurements of image signal. Output detector signal  $d(x)$  is represented by discrete values  $d_n$ , where each value corresponds to  $d(nx_0) = d(x)|_{x=nx_0}$ . The process of evaluating the values is called sampling.

Evaluating  $d(x)$  at positions  $x=ix_0$  corresponding to the centers of all detector elements can be represented as multiplication with the comb function:

$$\tilde{d}^+(x) = d(x) \sum_{i=-\infty}^{\infty} \delta(x - ix_0) = \sum_{i=-\infty}^{\infty} d_i \delta(x - ix_0) \quad (1.21)$$

which consists of an infinite train of  $\delta$  functions scaled by the detector values  $d_i$ . Multiplication with  $\sum_{i=-\infty}^{\infty} \delta(x - ix_0)$  in the spatial domain corresponds to convolution with  $(1/x_0) \sum_{i=-\infty}^{\infty} \delta(u - 1/ix_0)$  in the spatial-frequency domain:

$$F\{d^+(x)\} = D(u) * \frac{1}{x_0} \sum_{i=-\infty}^{\infty} \delta(u - \frac{1}{ix_0}) \quad (1.22)$$

Sampling  $d(x)$  at uniform spacing of  $x_0$  therefore corresponds to production of aliases of  $D(u)$  at spacings  $u=1/x_0$ . Overlapped aliases produce signal aliasing that caused image distortion at spatial frequencies below the sampling cut-off frequency,  $u_c = 1/(2x_0)$ .

Digital detector values are generated as a two-step process: integration of interacting input x-ray quanta in each detector element to produce a presampling detector signal and evaluation (sampling) of the presampling signal to generate the individual detector element values  $d_n$ . In the spatial frequency domain these two steps are described by presampling  $MTF_{pre}(u)$  and aliasing determined by the sample spacing  $x_0$ .

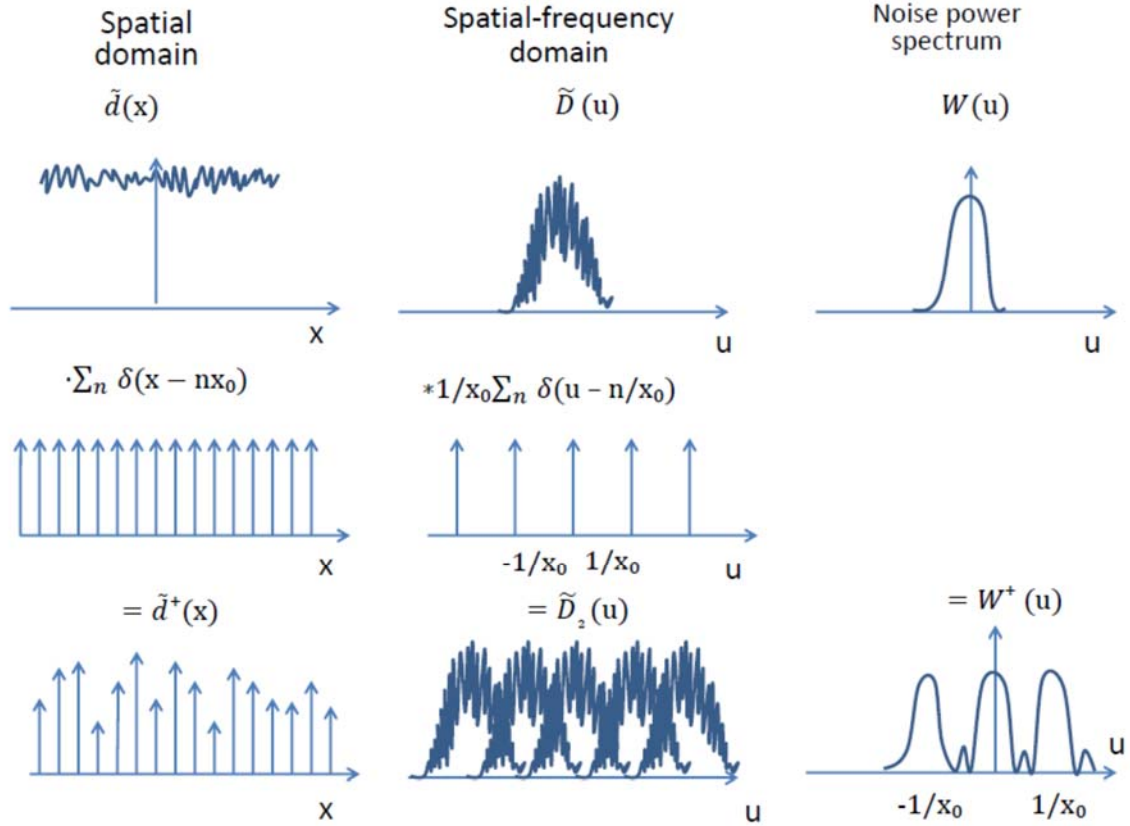


**Figure 1-7. Sampling a function at uniform spacings  $x_0$  causes spectral aliasing of the presampling signal if it contains frequency components above the sampling cut-off frequency  $u=1/x_0$ . We denote Wiener NPS as  $W(u)$  on CSA illustrations.**

A digital image consists of an array of discrete values  $d_n$ , which are samples of the detector presampling signal  $d(x)$ . The noise power spectrum of the process is given by:

$$NPS_{out}(u) = \frac{1}{x_0^2} NPS_{in}(u) * \sum_{-\infty}^{\infty} \delta\left(u - \frac{n}{x_0}\right) = \frac{1}{x_0^2} [NPS_{out}(u) + \sum_{n=1}^{\infty} NPS_{out}(u \pm \frac{n}{x_0})] \quad (1.23)$$

As can be seen from Eq. (1.20), the NPS of  $d^+(x)$  consists of a fundamental presampling NPS( $u$ ) as well as aliases centered at the frequencies  $u=n/x_0$ , scaled by the factor  $1/x_0^2$ . If the aliases overlap, noise aliasing increases image noise at frequencies below the sampling

cut-off frequency. According to the sampling theorem the frequencies above the cut-off frequencies  $u_c = 1/(2x_0)$  are not represented with samples of uniform sampling frequency  $u_s = 1/x_0$ . The NEQ is a measure of the noise equivalent number of quanta and is affected by noise aliasing. Signal aliasing adds artifacts that are not included in NEQ. The digital NEQ is defined only for frequencies less than the sampling cut-off frequency,  $u_c = 1/2x_0$ .

## 1.5 DQE improvement addressed in previous works

Improvements in image quality that can be obtained by reducing noise aliasing have been studied previously. For example, W.G. Ji et.al. [40] looked at reduction of aliasing in digital x-ray imaging for an amorphous selenium detector. They considered an “equivalent presampling filter” by digital image post-processing algorithms to attenuate frequency components at which noise aliasing was expected. They showed this reduced aliasing artifacts in images, but this approach also removed image structures at those same frequencies. Thus, while reducing image noise, their approach did not increase image SNR and therefore did not improve the DQE.

Another approach by the same authors [40] used an insulating layer between a-Se and the active matrix to introduce presampling image blurring. This modified imager was evaluated in terms of MTF, NPS and DQE to compare results with theoretical predictions. They concluded that noise aliasing can be reduced, or even eliminated, by physical blurring of image signals prior to collecting secondary quanta in the discrete detector elements, but at the expense of reduced MTF and decreased SNR caused by electronic noise due to a reduction in the measured signal. Even though presampling filtration makes an imaging system more susceptible to electronic noise, this approach could be used if detector sensitivity could be improved as long as the number of secondary quanta detected remains large to prevent introducing a secondary quantum sink.

In another study [41], imaging performance of a-Se based flat-panel detectors for digital mammography was considered using a small area prototype detector. They investigated DQE of a-Se flat panel detectors in theoretical and experimental ways. Theoretical model based on the cascaded linear system analysis with parallel processes in order to account for

fluorescence effect at the K-edge of a-Se (12.66 keV) within mammographic energy range. Their calculation showed that K fluorescence accounted for about 15% reduction of MTF at Nyquist frequency, while system NPS was reduced to 89% at zero spatial frequency. MTF evaluation showed additive blurring associated with charge trapping in a-Se layer that degraded presampling MTF and NPS at high spatial frequency and reduced noise aliasing. Accordingly, DQE approached 40% at zero spatial frequency.

Photon-counting detectors are currently under development as another approach to improving DQE. For example, a study on theoretical analysis of DQE of charge-sharing single-photon counting segmented silicon detectors [42] considered detector performance parameters, such as large area gain factor, presampling MTF, noise power spectra and DQE as functions of energy detection threshold. In his model of x-ray detector liberated charges could be shared between adjacent detector elements (pixels). Determining detective quantum efficiency of a monochromatic spectrum in terms of mean signal  $\bar{d}$ , presampling MTF and digital NPS using linear system analysis, DQE could be obtained as a combination:

$$DQE(u) = \frac{\bar{d}^2 |\text{MTF}_{\text{pre}}(u)|^2}{\bar{q}_0 \text{NPS}_{\text{dig}}(u)} \quad (1.24)$$

Therefore, DQE of a photon-counting detector can be expressed as a function of energy detection threshold and energy of incident x-ray quanta distribution. Transmission of detector signal and noise characteristics in entire x-ray detector is obtained through information from individual cascaded stages. The first stage of any x-ray imaging detector is an interaction of incident quanta with sensor material. Dimension of active portion of a detector element defines a detector aperture. Charge sharing effect was included in cascaded stages, which was expressed as a threshold energy dependency of an effective sampling aperture. The model was developed for a simple one-dimensional detector with the possibility for charge sharing events between adjacent detector elements. Proposed approach can be used to study charge-sharing effects on image quality for single photon counting x-ray detectors with small semiconductor pixels. It was noticed that charge

sharing degrades output detector characteristics and results in increased image noise in proposed x-ray detector model.

Cascaded approach evaluation of DQE for photon counting detectors was described previously by J. Tanguay et. al. [43] in order to improve image quality in implementation of an advanced energy-dependent x-ray imaging. Cascaded system analysis was used to define DQE of proposed direct-conversion selenium (Se) and cadmium zinc telluride (CdZnTe) detectors including different effects of poly-energetic spectra. In their work they found that single photon counting DQE was 5-20% greater than that of conventional energy-integrating detectors for any given x-ray energy range and convertor thickness. Nevertheless, DQE of single-phonon counting models as well as energy-integrating x-ray detectors is decreased due to negative factors, e.g. weak collection efficiency and significant additive noise.

In another study [44] on design and optimization of imaging detector with radiotherapy application, the authors investigate performance of thin-film cadmium telluride large-area x-ray detector in photovoltaic application to develop optimal parameters of detector model with high DQE at energy reabsorption and signal-to-noise spatial spreading. In indirect detection detectors, thin-film semiconductor complements scintillator converting incoming x-ray quanta into optical photons, registered in amorphous silicon photodiodes that generate a digital output detector signal. The problem arises with poor absorption of x-rays leading to low quantum efficiency. They propose to increase by improving x-ray absorption with very thick ( $>10$  mm) detection material. It can be implemented by segmentation with crystalline scintillator coupled with a-Si photodiode array or by x-ray focusing with fiber matrix or microstructured plates with purpose to mitigate signal spreading. These systems are considered to be very expensive for practical implementation. An alternative cost-effective approach is a use of high electron density semiconductor thin layer in a direct detection design. Recently, CdTe and CdZnTe structures with thickness 200 – 300  $\mu\text{m}$  were implemented for kV imaging overgrowing common a-Si structures. Authors proposed a simple direct conversion model, combining thin-film CdTe with a metal plate that enhances x-ray energy absorption. In terms of

theoretical analysis of signal and noise propagation, an imaging system described with CSA approach consists of the following stages:

- 1) X-ray interaction in metal converter (CdTe), which outcomes in energy deposition by scattered charges (Compton scattering)
- 2) Stochastic blurring in metal converter (CdTe)
- 3) Quantum gain due to formation of e-h pairs
- 4) Addition noise, attributable to dark current in semiconductor
- 5) Integration of charges in discrete pixel elements; deterministic blur is introduced into system on this stage due to geometrical difference of pixel aperture size
- 6) Readout of imaging signal by acquisition electronics

Detector performance is evaluated in terms of the DQE. Stochastic processes of each process in the CSA model result in random noise in the generated image. Ratio of squared output signal-to-noise to input squared signal-to-noise determines DQE of an imaging system [45].  $DQE(0)$  is a component associated with quantum absorption process, the rest non-zero frequency components  $DQE(u)$  are associated with signal spreading in the detector. Quantum absorption and therefore energy deposition in detector materials are characterized in terms of quantum gain in conversion layer of a detector, which can be evaluated with Monte Carlo simulation as a ratio of number of photons depositing energy in convertor layer to the total number of incident quanta. As the stochastic blurring in metal converter starts to contribute on the next stage, frequency-dependent  $DEQ(u)$  was evaluated in terms of average deposited energy  $E$ , spatial distribution of incident quanta, modulation transfer function  $MTF(u)$  and noise power spectrum of absorbed quanta within a thin-film CdTe layer of detector. X-rays interacting in a metal layer produce ionizing electrons and positrons, which liberate electron-hole pairs in CdTe layer through numerous individual reactions along trajectory of each ionizing particle. Energy deposition locations associated with these interactions contribute to correlated quantum noise. This will determine the following gain stage, which is associated with conversion of deposited x-ray

energy into charge carrier pairs in a convertor layer. Quantum amplification is evaluated based on ionization energy  $W$  of convertor material, its thickness and amount of energy deposited by incoming quanta in a convertor,  $E_d$ :

$$g = \frac{E_d}{W} \quad (1.25)$$

In a nutshell, considered thin-film CdTe based detector systems were claimed to have the following advantages: 1) CdTe-based systems provide higher efficiencies due to high atomic number and direct detection design in comparison with the parameters of commercial phosphor/amorphous silicon or selenium based detectors; 2) it's technically easier to implement a large-area device by means of continuous thin-film deposition; 3) shorter development time and lower cost. The authors concluded that large-area CdTe film-based detector have a promising application for radiation therapy imaging.

Finally, a study by El-Mohri, et. al. considered optimization of segmented scintillators performance by a binning technique [46]. Misalignment in current segmented scintillators creates difficulties in optimal registration with active matrix flat-panel imaging arrays, which result in degradation of image spatial resolution. As a solution, it was proposed high resolution active flat-panel matrix array in combination with the binning technique, described in that paper. An array, consisting of 0.127 mm pixels, is coupled to a segmented scintillators based on BGO, LYSO and CsI:TI materials of thickness about 10 mm. For every proposed prototype, 8x8 pixel binning was performed to achieve a sampling pattern of 1.016 mm size optimized by alignment metric, which reduces misregistration and therefore improve spatial resolution. Such approach resulted in improving of spatial resolution for BGO and LYSO prototypes, but not for CsI prototype due to significant cross talk resulting from light quanta scattering between scintillator elements. The efficacy of binning techniques in terms of improving spatial resolution was proved for scintillator materials with high density, mechanical hardness and high reflective index, such as BGO scintillator. Materials exhibiting these properties as well as high quanta output, such as  $\text{CdWO}_4$ , are suggested to provide additional preserving of DQE performance. However, at high spatial frequencies DQE degrades and the problem remains unresolved.

While these approaches have helped improve our understanding of detector performance and DQE improvements, they have not reduced the overall effect of noise aliasing while maintaining the aperture MTF. As a result, the damaging effect of noise aliasing on high-frequency values of the DQE remains unsolved.

## 1.6 Description of proposed solution (AAP)

The target of this research project is to address the problem of improving DQE of an x-ray detector at high spatial frequencies by developing a detector design with improved performance using cascaded systems analysis. In order to achieve this goal, an apodized aperture pixel (AAP) x-ray detector design is proposed and validated. We considered signal and noise propagation in AAP x-ray detector at each stage AAP-design (development of cascaded model) to study system characteristics contributing to DQE of imaging system to ensure improvement. AAP model was developed based on idea of very small detector elements (CMOS coupled with a-Se), which permits high spatial resolution and therefore fine image details conservation in a detector output (i.e. resultant x-ray image) [25].

## 1.7 Brief overview of the thesis

This thesis consists of four chapters. The above *Introduction* briefly summarizes theoretical framework and short overview of previous studies associated with efforts to improve the DQE of imaging detectors.

*Chapter 2* is based on the published article “Apodized-Aperture Pixel Design to Increase High-Frequency DQE and Reduce Noise Aliasing in X-Ray Detectors”, Elina Ismailova, Karim Karim and Ian A. Cunningham, Proc. SPIE Medical Imaging, The Physics of Medical Imaging, 9412-12 (2015). It describes development of our proposed AAP x-ray detector with improved high frequency DQE component including an experimental proof-of-concept validation on a laboratory CMOS/CSI detector.

*Chapter 3* describes a numerical approach to optimizing the AAP design in an iterative approach to obtain an optimal linear filter used to synthesis image pixels.



Finally, *Chapter 4* is devoted to discussion and conclusions of performed study to address the achievements with the developed AAP x-ray detector and to draw future directions with AAP detector design.

## 1.8 References

1. G. Neta, P. Rajaraman, A. Berrington de Gonzalez, M. M. Doody, B. H. Alexander, D. Preston, S. L. Simon, D. Melo, J. Miller, D. M. Freedman, M. S. Linet and A. J. Sigurdson, "A prospective study of medical diagnostic radiography and risk of thyroid cancer," *Am J Epidemiol*, 2013. **177**(8): p. 800-809.
2. M. Périard, P. Chaloner, "Diagnostic X-ray imaging quality assurance: an overview," *Can J Med Rad Tech*, 1996. **27**: p. 171-177.
3. M. S. Linet, T. L. Slovis, D. L. Miller, R. Kleinerman, C. Lee, P. Rajaraman, A. Berrington de Gonzalez, "Cancer risks associated with external radiation from diagnostic imaging procedures," *Can Cancer J Clin*, 2012. **62**(2): p. 75-100.
4. E.J. Calabrese, M.K. O'Connor, "Estimating risk of low radiation doses-a critical review of the BEIR VII Report and its use of the linear no-threshold (LNT) hypothesis," *Radiat Res*, 2014. **182**(5): p. 463-474.
5. S. Yoshino, K. Miki, K. Sakata, Y. Nakayama, K. Shibayama, S. Mori, "Digital reconstructed radiography with multiple color image overlay for image-guided radiotherapy," *J Radiat Res*, 2015. **56**(3): p.588-593.
6. V. Neofotistou, V. Tsapaki, S. Kottou, A. Schreiner-Karoussou, E.Vano, "Does digital imaging decrease patient dose? A pilot study and review of the literature," *Radiat Prot Dosimetry*, 2005. **117**(1-3): p. 204-210.
7. J.A. Seibert, "Digital radiography: The bottom line comparison of CR and DR technology," *Appl Radiol*, 2009. **38**(5): p. 21-28.
8. F. Lacroix, L. Beaulieu, L. Archambault, A.S. Beddar , "Simulation of the precision limits of plastic scintillation detectors using optimal component selection," *Med Phys*, 2010. **37**(2): p. 412-418.
9. H.G. Chotas, C.E. Ravin, "Digital radiography with photostimulable storage phosphors. Control of detector latitude in chest imaging," *Invest Radiol*, 1992. **27**(10): p. 822-828.
10. J.A. Seibert, J.M. Boone, V.N. Cooper, K.K. Lindfors, "Cassette-based digital mammography," *Technol Cancer Res Treat*, 2004. **3**(5): p. 413-427.

11. M. Bertolini, A. Nitrosi, S. Rivetti, N. Lanconelli, P. Pattacini, V. Ginocchi, M. Iori, "A comparison of digital radiography systems in terms of effective detective quantum efficiency," *Med Phys*, 2012. **39**(5): p. 2617-2627.
12. N.M. Allinson, "Development of Non-Intensified Charge-Coupled Device Area X-ray Detectors," *J Synchrotron Radiat*, 1994. **1**(Pt 1): p. 54-62.
13. I.A. Cunningham, M.S. Westmore, A. Fenster, "A spatial-frequency dependent quantum accounting diagram and detective quantum efficiency model of signal and noise propagation in cascaded imaging systems," *Med Phys*, 1994. **21**(3): p. 417-427.
14. T. Yu, J.M. Sabol, J.A. Seibert, J.M. Boone, "Scintillating fiber optic screens: a comparison of MTF, light conversion efficiency, and emission angle with Gd<sub>2</sub>O<sub>2</sub>S:Tb screen," *Med Phys*, 1997. **24**(2): p. 279-285.
15. K. Uesugi, M. Hoshino, N. Yagi, "Comparison of lens-and fiber-coupled CCD detectors for X-ray computed tomography," *J Synchrotron Radiat*, 2010. **18**(2): p. 217-223.
16. D.M. Hunter, G Belev, S Kasap, M.J. Yaffe, "Measured and calculated K-fluorescence effects on the MTF of an amorphous-selenium based CCD x-ray detector," *Med Phys*, 2012. **39**(2): p. 608-622.
17. J.R. Scheuermann, A.H. Goldan, O. Tousignant, S. Léveillé, W. Zhao, "Development of solid-state avalanche amorphous selenium for medical imaging," *Med Phys*, 2015. **42**(3): p. 1223-1226.
18. M.M. Wronski, J.A. Rowlands, "Direct-conversion flat-panel imager with avalanche gain: feasibility investigation for HARP-AMFPI," *Med Phys*, 2008. **35**(12): p. 5207-5218.
19. Y. El-Mohri, L.E. Antonuk, M. Konieczek, Q. Zhao, Y. Li, R.A. Street, J.P. Lu, "Active pixel imagers incorporating pixel-level amplifiers based on polycrystalline-silicon thin-film transistors," *Med Phys*, 2009. **36**(7): p. 3340-3355.
20. L.E. Antonuk, Y. El-Mohri, W. Huang, K.W. Jee, J.H. Siewerdsen, M. Maolinbay, V.E. Scarpine, H. Sandler, J. Yorkston, "Initial performance evaluation of an indirect-detection, active matrix flat-panel imager (AMFPI) prototype for megavoltage imaging," *Int J Radiat Oncol Biol Phys*, 1998. **42**(2): p. 437-454.
21. J.S. Seo, B.S. Bae, "Improved electrical performance and bias stability of solution-processed active bilayer structure of indium zinc oxide based TFT," *ACS Appl Mater Interfaces*, 2014. **6**(17): p. 15335-15343.

22. M. Wronski, W. Zhao, K. Tanioka, G. Decrescenzo, J.A. Rowlands JA, "Scintillator high-gain avalanche rushing photoconductor active-matrix flat panel imager: zero-spatial frequency x-ray imaging properties of the solid-state SHARP sensor structure," *Med Phys*, 2012. **39**(11): p. 7102-7109.
23. S.S. Nagesh, R. Rana, M. Russ, C. Ionita, D. Bednarek, S. Rudin, "WE-G-204-04: Focal Spot Deblurring For High Resolution Amorphous Selenium (aSe) Complementary Metal Oxide Semiconductor (CMOS) X-Ray Detector," *Med Phys*, 2015. **42**(6): p. 3694.
24. M.A. Baysal, E. Toker, "CMOS cassette for digital upgrade of film-based mammography systems," *Med Imag Int Soc Opt Phot.*, 2006. **6142**(3): p. 770-781
25. C.C. Scott, S. Abbaszadeh, S. Ghanbarzadeh, G. Allan, M.Farrier, I.A. Cunningham, K.S. Karim, "Amorphous selenium direct detection CMOS digital x-ray imager with 25 micron pixel pitch," *SPIE Med Imag Int Soc Opt Phot* 2014. **9033**(11): p. 1605-1611.
26. L. Timmermans, A. De Hauwere, K. Bacher, H. Bosmans, K. Lemmens, L. Bleyen, E. Van Limbergen, P. Martens, A. Van Steen, G. Mortier, K. Van Herck, H. Thierens, "Impact of the digitalisation of mammography on performance parameters and breast dose in the Flemish Breast Cancer Screening Programme," *Eur Radiol*, 2014. **24**(8): p. 1808-19.
27. N.T. Ranger, E. Samei, J.T. Dobbins, C.E. Ravin, "Assessment of detective quantum efficiency: Intercomparison of a recently introduced international standard with prior method," *Radiology*, 2007. **243**(3): p. 785-795.
28. R. Shaw, "The equivalent quantum efficiency of the photographic process," *J. Photogr. Sci*, 1963. **11**(199-204).
29. J. Dainty, R. Shaw, "Image Science," Academic, New York, 1974. Ch. 2: p. 39-42.
30. I.A.Cunningham, "Applied linear-systems theory," *Handbook of medical imaging*, 2000. **1**: p. 79-159.
31. R. Akbarpour, S.N. Friedman, J.H. Siewerdsen, J.D. Neary, I.A. Cunningham IA, "Signal and noise transfer in spatiotemporal quantum-based imaging systems," *J Opt Soc Am A Opt Image Sci Vis*, 2007. **24**(12): p. 151-164.
32. M. Rabbani, R. Shaw, R. Van Metter, "Detective quantum efficiency of imaging systems with amplifying and scattering mechanisms," *JOSA A*, 1987. **4**(5): p. 895-901.
33. M. Rabbani, R. Van Metter, "Analysis of signal and noise propagation for several imaging mechanisms," *JOSA A*, 1989. **6**(8): p. 1156-1164.

34. P.C. Bunch, K.E. Huff, R. Van Metter, "Analysis of the detective quantum efficiency of a radiographic screen-film combination," *JOSA A*, 1987. **4**(5): p. 902-909.
35. G. Hajdok, J. Yao, J.J. Battista, I.A. Cunningham, "Signal and noise transfer properties of photoelectric interactions in diagnostic x-ray imaging detectors," *Med Phys*, 2006. **33**(10): p. 3601-3620.
36. S.N. Friedman, I.A. Cunningham, "A spatio-temporal detective quantum efficiency and its application to fluoroscopic systems," *Med Phys*, 2010. **37**(11): p. 6061-6069.
37. S. Yun, J. Tanguay, H.K. Kim, I.A. Cunningham, "Cascaded-systems analyses and the detective quantum efficiency of single-Z x-ray detectors including photoelectric, coherent and incoherent interactions," *Med Phys*, 2013. **40**(4): p. 916-923.
38. J. Xu, W. Zbijewski, G. Gang, J.W. Stayman, K. Taguchi, M. Lundqvist, E. Fredenberg, J.A. Carrino, J.H. Siewerdsen, "Cascaded systems analysis of photon counting detectors," *Med Phys*, 2014. **41**(10): p. 101-115.
39. M.F. Kijewski, Judy, "The noise power spectrum of CT images," *Phys Med Biol*, 1987. **32**(5): p. 565-575.
40. W.G. Ji, W. Zhao, J.A. Rowlands, "Digital x-ray imaging using amorphous selenium: reduction of aliasing," *Med Phys*, 1998. **25**(11): p. 2148-2162.
41. W. Zhao, W.G. Ji, A. Debie, J.A. Rowlands, "Imaging performance of amorphous selenium based flat-panel detectors for digital mammography: characterization of a small area prototype detector," *Med Phys*, 2003. **30**(2): p. 254-263.
42. S.R. Amendolia, M.G. Bisogni, P. Delogu, M.E. Fantacci, G. Paternoster, V. Rosso, A. Stefanini, "Characterization of a mammographic system based on single photon counting pixel arrays coupled to GaAs x-ray detectors," *Med Phys*, 2009. **36**(4): p. 1330-1339.
43. J. Tanguay, S. Yun, HK Kim, I.A. Cunningham, "The detective quantum efficiency of photon-counting x-ray detectors using cascaded-systems analyses," *Med Phys*, 2013. **40**(4): p. 913-926.
44. E.I. Parsai, D. Shvydka, J. Kang, "Design and optimization of large area thin-film CdTe detector for radiation therapy imaging applications," *Med Phys*, 2010. **37**(8): p. 3980-3994.
45. T. Michel, G. Anton, M. Böhnel, J. Durst, M. Firsching, A. Korn, B. Kreisler, A. Loehr, F. Nachtrab, D. Niederlöhner, F. Sukowski, P. Takoukam Talla, "A fundamental method to determine the signal-to-noise ratio (SNR) and detective

quantum efficiency (DQE) for a photon counting pixel detector," *Nuc Ins Meth in Phys Res A: Accelerators, Spectrometers, Detectors and Associated Equipment*, 2006. **568**(2): p. 799-802.

46. Y. El-Mohri, L.E. Antonuk, R.B. Choroszuca, Q. Zhao, H. Jiang, L. Liu, "Optimization of the performance of segmented scintillators for radiotherapy imaging through novel binning techniques," *Phys Med Biol*, 2014. **59**(4): p. 797-818.

## Chapter 2

### 2 AAP detector design

This material was presented in the SPIE conference proceedings article “Apodized-Aperture Pixel Design to Increase High-Frequency DQE and Reduce Noise Aliasing in X-Ray Detectors”, Elina Ismailova, Karim Karim and Ian A. Cunningham, Proc. SPIE Medical Imaging, The Physics of Medical Imaging, 9412-12 (2015).

#### 2.1 Introduction

The known risks associated with exposure to radiation [[1-3](#)] is a key motivator for the development of new detector technologies with the goal of producing better images for lower patient exposures. In diagnostic radiology, reducing patient exposures generally results in reduced image signal-to-noise ratio (SNR). The ability to see structures in a noise-limited image is described by the detectability index [[4](#), [5](#)] defined as the product of the image noise-equivalent number of quanta (NEQ) [[6](#), [7](#)] and the squared Fourier transform of the image structure to be visualized, integrated over spatial frequencies. For a given task, therefore, detectors must be designed to optimize the NEQ over spatial frequencies of importance.

The NEQ describes the effective number of x-ray quanta used by the detector to generate an image, and low noise images correspond to high NEQ values. The NEQ is determined by the number of x-ray quanta incident on a detector and the detective quantum efficiency (DQE), where the DQE is the effective quantum efficiency of the detector [[6](#)]. Thus, improvements in image quality and/or reductions of radiation exposure require maximizing the DQE over all spatial frequencies of importance for the task.

A great deal of effort has been devoted to increasing the zero-frequency DQE value of new detectors. For example, zero-frequency DQE values of mammography systems have increased from 0.3-0.5 for film-screen systems [[8-10](#)] to  $\sim 0.8$  for new high-performance flat-panel digital detectors. We therefore suggest there is little room for further improvements in the zero-frequency DQE value and future research efforts should now

focus on improving high-frequency values of the DQE (anticipated benefits from photon-counting detectors are not included in this comment [11].

Digital detectors generally consist of a converter layer (e.g. scintillator such as CsI or semiconductor such as Se) coupled to an electronic sensor array. The sensor array produces a signal from each element that is proportional to the number of secondary quanta incident on the element. Signal and noise properties of these detectors, including the DQE, can be described using cascaded-systems theory [12, 13-17]. At mammographic energies where all x-ray photons have energies below the K-edge energy of the converter, the DQE frequency response is determined primarily by scatter of secondary quanta and noise aliasing [14]. The best spatial resolution is obtained with selenium-based systems where secondary scatter is negligible. In this study, we propose a novel method for improving the high-frequency DQE of all x-ray detectors, and in particular for Se-based detectors for mammography.

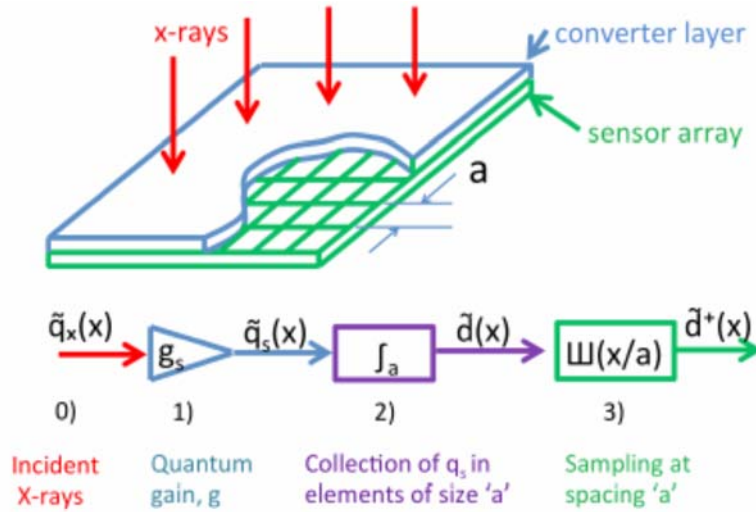


**Figure 2-1. Schematic illustration of a conventional detector, consisting of a conversion layer where interacting x-ray quanta are converted to secondary quanta, such as light from a scintillator or liberated charges from a photoconductor, and a sensor array to collect secondary quanta. The sensor array consists of a two-dimensional array of elements having dimension  $a$ . The corresponding cascaded model consists of: 0) spatial distribution of incident x-ray quanta  $\tilde{q}_x(x)$ ; 1) conversion**

to secondary quanta  $\widetilde{q}_x(x)$ ; 2) integration of secondary quanta in sensor elements giving detector presampling signal  $\widetilde{d}(x)$ ; 3) sampling at centers of elements giving a sequence of Dirac  $\delta$ -functions scaled by detectors output signals,  $\widetilde{d}^+(x)$ .

## 2.2 Methods

The DQE of digital detectors is normally expressed as a function of spatial frequency up to the sampling cutoff frequency  $u_c$  where  $u_c = 0.5/a$  [cycles/mm] and  $a$  [mm] is the width of one sensor element. When spatial spreading of secondary scatter is negligible and the modulation transfer function (MTF) is determined primarily by the pixel aperture size (such as with selenium-based detectors), the DQE can be described using the cascaded systems approach as

$$DQE(u) = \frac{|T(u)|^2}{X Q_0 W(u)/d^2} = DQE(0) \text{sinc}^2(au) \quad (2.1)$$

where detector readout noise is assumed small, the MTF is equal to  $|T(u)| = |\text{sinc}(au)|$ ,  $X$  is the x-ray exposure incident on the detector,  $Q_0$  is the number of x-ray quanta/mm<sup>2</sup> per unit exposure,  $d$  is the average dark subtracted pixel value in uniform images having Wiener noise power spectrum (NPS) $W(u)$  which is proportional to  $\text{sinc}^2(au)$ . In this example, the DQE value falls to the fraction  $\text{sinc}^2(au_c) = \text{sinc}^2(0.5) = 4/\pi^2 \approx 0.41$  relative to the zero-frequency value due to noise aliasing alone. This results in additional high-frequency noise that gives images from selenium-based detectors their characteristic high-frequency noise structure.

### 2.2.1 Conventional Detector Design

A simple illustration of a “conventional” Se-based detector is shown in Fig. 2-1. X-ray photons interact in a converter layer to produce secondary quanta (liberated charge carriers). The secondary quanta are accumulated in discrete sensor elements of width  $a$  in a sensor array and there is a direct correspondence of sensor elements to image pixels.



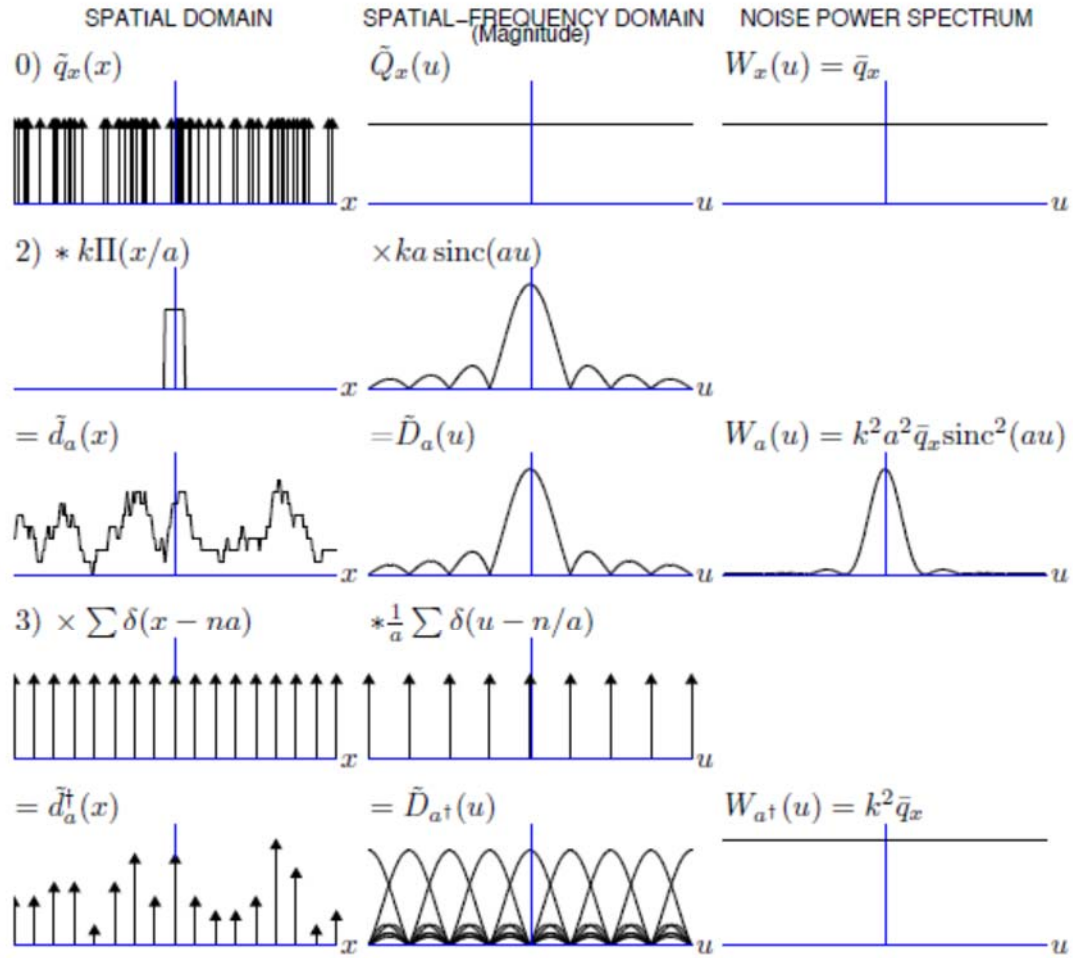


**Figure 2-2. Illustration of signal and noise transfer through a conventional detector in spatial and spatial-frequency domains. Conversion to secondary quanta in step 1 has been omitted for brevity. The input,  $\tilde{q}_x(x) = \sum_i \delta(x - x_i)$ , is a random distribution of x-ray quanta incident on the detector input, represented as a distribution of Dirac  $\delta$ -functions. The output is  $\tilde{d}_a(x)$ , a set of regularly – spaced  $\delta$ -functions on spacing  $a$ , scaled by the corresponding image pixel values.**

The signal and noise properties of this detector are illustrated (in one dimension for simplicity) in Fig. 2-2. In this model, a random spatial distribution of x-ray quanta  $\tilde{q}_x(x)$  (the overhead  $\sim$  is used to indicate a random variable) is incident on the converter layer

$$\tilde{q}_x(x) = \sum_i \delta(x - \tilde{x}_i) \quad (2.2)$$

and  $\tilde{x}_i$  is a random variable describing the position of the  $i$ th incident photon. It is assumed each photon interacts to produce a fixed number of secondary quanta (deterministic gain), resulting in a distribution of secondary quanta  $\tilde{q}_x(x)$ . Deterministic gain does not affect the DQE, so we assume unity gain with no subsequent scatter of secondary quanta in Fig. 2-2 for simplicity. All secondary quanta are collected by the sensor array in elements of width  $a$ . This is represented as a convolution of  $\tilde{q}_x(x)$  with the rectangle function  $\Pi(x/a)$ , scaled by the factor  $k$  that relates detector output signal to the average number of incident x-ray quanta per unit area  $\bar{q}(x)$ , resulting in the detector presampling signal  $\tilde{d}_a(x)$ . While not physical,  $\tilde{d}_a(x)$  is a function that, when evaluated at positions corresponding to the centres of physical sensor elements, gives the physical sensor output values. Thus, the resulting detector signal is described as

$$\tilde{d}_a^+(x) = \sum_n \left[ \tilde{q}_x(x) * k\Pi\left(\frac{x}{a}\right) \right] \delta(x - na) = \sum_i \tilde{d}_{a,n} \delta(x - na) \quad (2.3)$$

where  $\tilde{d}_a^+(x) = \tilde{q}_x(x) * k\Pi(x/a)$   $\tilde{d}_{a,n}$  is the signal from the  $n$ th sensor element, and  $\tilde{d}_a^+(x)$  is a series of  $\delta$ -functions on spacing  $a$  scaled by  $\tilde{d}_{a,n}$ .

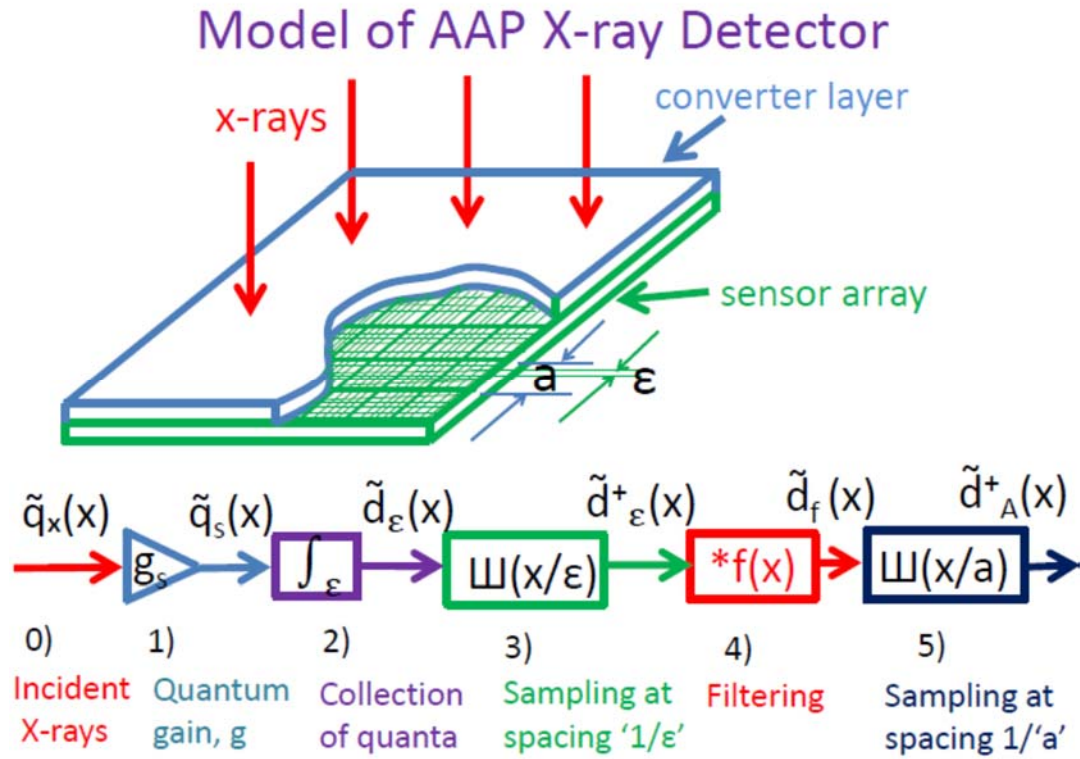


**Figure 2-3. Schematic illustration of an apodized-aperture pixel structure.** It differs from the conventional detector by using very small sensor elements of dimension  $\epsilon$  and filter  $f(x)$  to synthesize the detector presampling signal  $\tilde{d}f(x)$ . The sinc-shaped filter prevents noise aliasing while preserving the superior frequency response of the small elements, resulting in improved DQE.

The frequency response of the detector is illustrated in the center column. In the bottom row,  $\tilde{D}_a^+(u)$  consists of the fundamental frequency spectrum and overlapping aliases resulting from sampling in step 3. The fundamental has a  $\text{sinc}^2$  shape. Overlap of aliases is responsible for signal aliasing and appears as a complicated overlap of lines close to the frequency axis. It is seen from Fig. 2-2 that while the Wiener NPS of  $\tilde{d}_a(x)$ ,  $W_a(u)$ , is proportional to  $\text{sinc}^2$  at step 2, aliasing results in a frequency-independent NPS and as a result the DQE is proportional to  $\text{sinc}^2$ .

### 2.2.2 Apodized Aperture Pixel (AAP) design

We propose a method of creating apodized apertures with the goal of increasing high-frequency DQE values as illustrated in Fig.2-3. The method requires the use of sensor arrays having sensor elements of size  $\epsilon$  much smaller than the desired pixels of size  $a$ . This could be achieved, for example, using a CMOS sensor array that can have elements as small as 10 - 25  $\mu\text{m}$  [16]. While this corresponds to a sampling cut-off frequency of 20 - 50 cycles/mm, it is unlikely this high resolution will have any clinical significance and the patient exposure required to achieve high SNR in such images would likely be prohibitive in most applications. In addition, the workloads in radiology departments would make the archival, transmission and display (if that were even possible) of such large image files prohibitive. We propose digitizing and processing sensor-element data either directly on the sensors or as post-processing within the imaging system, to synthesize larger image pixels using an algorithm that will reduce noise aliasing and thereby increase the DQE. This approach will be most effective if the converter layer has very high spatial resolution (no spatial spreading of secondary quanta) such that resolution is largely determined by element size, even with the small elements. Thus, selenium may be a preferable converter, although some benefit may be achieved with other converters as well.

Simple binning of small sensor elements does not increase the DQE at the sampling cut-off frequency in our cascaded model. Regardless of the number of elements binned or element size, the DQE at  $u_c$  remains less than half of the zero-frequency value due to the  $\text{sinc}^2$  shape.

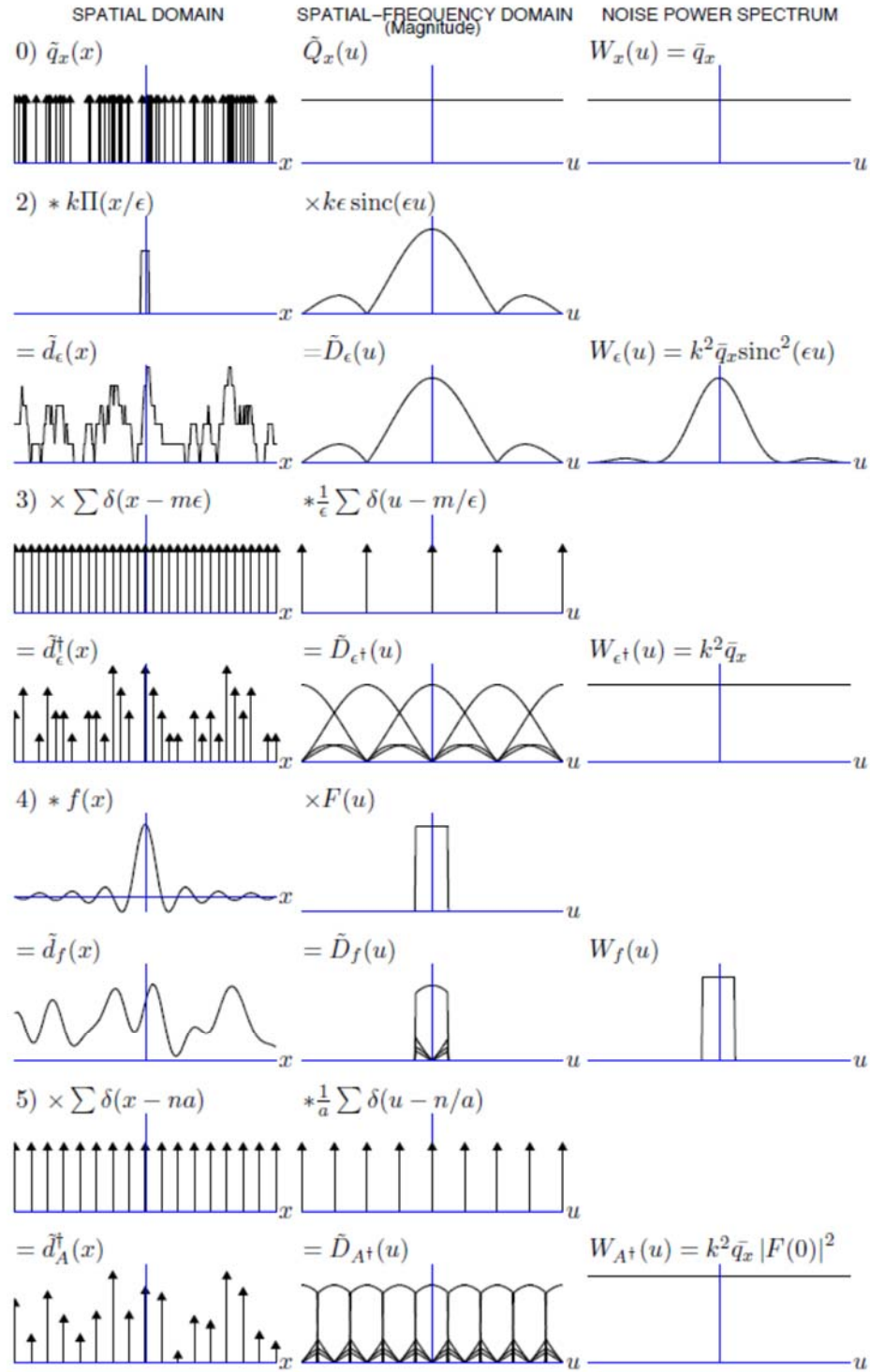
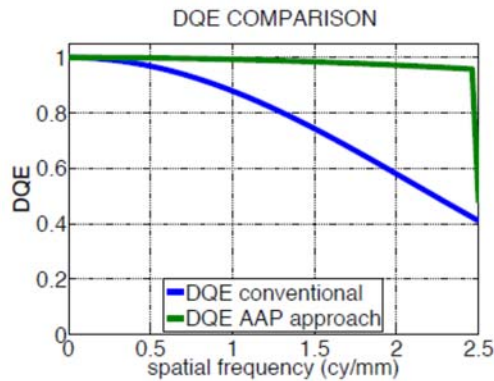


Figure 2-4. Illustration of signal and noise transfer through the apodized-aperture pixel design in spatial and spatial frequency domains. Step 1, conversion to secondary quanta in the converter, has been omitted for brevity. The output  $\tilde{d}_A^\dagger(x)$  is similar to

that of the conventional detector except pixel values are synthesized from detector element signals as a convolution with  $f(x)$  at step 4). By choosing  $f(x) = \text{sinc}(au)$ , the effect of noise aliasing on the DQE is greatly reduced as illustrated here.

To improve the DQE we propose an apodized-aperture pixel (AAP) design in which data is acquired in sensor elements of size  $\varepsilon$  and then processed to synthesize image pixels of size  $a$ . The sensors must have extremely low readout noise to ensure a high DQE value, something else that can be achieved with CMOS sensors. The signal and noise characteristics in both spatial and spatial frequency domains are illustrated in Fig. 2-4. Steps 1 and 2 are the same as the conventional detector except for the use of very small sensor elements having dimension  $\varepsilon$ . In the AAP design, data from the small elements,  $\tilde{d}^+_{\varepsilon}(x)$ , is subsequently convolved with a filter kernel  $f(x)$  to generate a presampling function  $\tilde{d}(x)$ , which is subsequently evaluated at spacings  $a$  to generate the output signal consisting of a sequence of Dirac  $\delta$  functions on spacings  $a$  scaled by the discrete detector output values. In practice, the discrete values are synthesized by a numerical convolution of the discrete values from each small element with a discrete vector  $f_i$ .



**Figure 2-5. Comparison of conventional and apodized DQE as determined for ideal x-ray converter using the CSA model with physical elements of width  $\varepsilon = 0.05$  mm and image pixels of width  $a = 0.2$  mm. The DQE is almost independent of spatial frequency and is doubled at the sampling cut-off frequency.**

The AAP approach was validated experimentally using a high-resolution CMOS-based detector with a CsI converter (Xmaru, Rayence Co. Ltd., Seoul Korea). Using data from

physical sensor elements with dimension  $e = 0.050$  mm, images required to measure the detector DQE were generated by: a) binning  $4 \times 4$  elements to simulate a conventional detector with elements, having width  $a = 0.20$  mm; and b) synthesizing image pixels on spacing of  $a = 0.20$  mm using the AAP approach with  $256 \times 256$  sinc-shaped kernel  $f$ . Exposure data was acquired on a lab-based x-ray system using an RQA-5 spectrum with  $0.66$  mR ( $5.8 \mu\text{Gy}$  air KERMA) incident on the detector. The DQE test instrument *DQEPro* was used for data acquisition and analysis.

## 2.3 Results

The utility of the illustrations in Figs. 2-2 and 2-4 is they provide the frequency response of both signal and noise that can be obtained with each method, including the DQE. The benefits of the AAP approach can be determined by comparing these two figures as they are plotted with the same spatial and spatial-frequency scales. The left column in each figure shows propagation of the same random distribution of incident x-ray quanta. The frequency response of the small elements is much broader than that of larger elements, seen by comparing  $\tilde{D}_e(u)$  at step 2 in Fig. 2-4 with  $\tilde{D}_a(u)$  at step 2 in Fig. 2-2. By choosing the sinc-shaped kernel  $f(x) = \text{sinc}(x/a)$  shown in Fig. 2-4, we obtain a low-pass filter that passes frequencies below the image cut-off frequency  $u = 0.5/a$  with equal weighting while blocking all frequencies above. This increases the DQE by preserving the superior frequency response of the small elements (aperture MTF) and reducing noise aliasing.

The output image signal and noise are illustrated in the bottom row. While both detector designs have the same number of image pixels, and on the same spacings, pixel values of the AAP detector  $\tilde{d}^+ A(x)$  differ to those of the conventional detector  $\tilde{d}^+_a$  in subtle ways due to differences in frequency response and the reduction of signal aliasing. The frequency response of each is seen in the central column where  $\tilde{D}^+_A(x)$  has a more uniform fundamental spectral component compared to the conventional detector. In addition, there is less overlap of higher-order aliases which is responsible for the reduced signal aliasing. Similar to the conventional detector, the Wiener NPS is also independent of frequency. Thus, the appearance of noise in a selenium-based AAP image would be unchanged, even

though aliasing is largely reduced. Rather, the MTF is improved, resulting in a DQE improvement.

Figure 2-5 shows a comparison of the DQE obtained using the AAP approach ( $\epsilon=0.05\text{mm}$ ) with a conventional detector ( $a=0.2\text{ mm}$ ). There is no difference in the zero-frequency DQE value while the high-frequency DQE value is increased by a factor of almost 2.5.

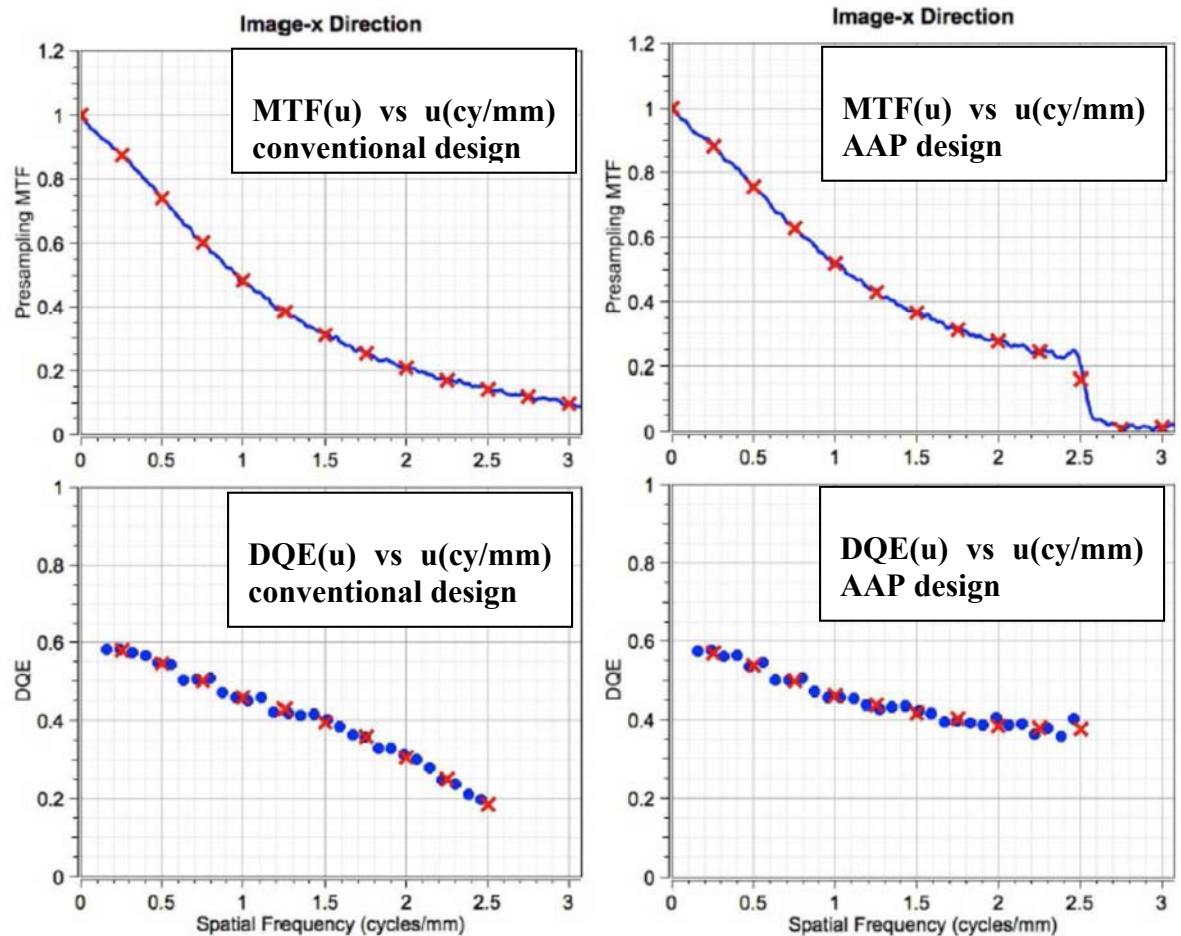


**Figure 2-6. Experimental validation of the AAP concept using a CMOS/CsI-based detector (Xmaru, Rayence Co.) with physical sensor elements of 0.05 mm (RQA-5 spectrum, 0.66 mR detector exposure). Left: Presampling MTF and DQE obtained using images constructed by 4x4 binning of detector data to simulate a conventional detector with 0.2-mm elements. Right: Presampling MTF and DQE obtained using images synthesized using the AAP approach to create 0.2-mm pixels. The MTF is increased at frequencies above 1.5 cycles/mm and all frequencies above 2.5 cycles/mm**



**are removed from the image. The high-frequency DQE is increased from 0.2 to 0.4. Blue curves – experimental data, red points – estimates at spacing 0.25 cy/mm.**

Figure 2-6 shows the results of the experimental validation of the AAP concept on a CMOS/CsI-based detector. The left column shows MTF and DQE curves measured using images in which 0.05-mm sensor elements were binned 4x4 to simulate a conventional detector with 0.2-mm elements. The right column shows the MTF and DQE obtained using the AAP approach to synthesize 0.2-mm image pixels from 0.05-mm physical sensor elements. The MTF is raised at frequencies above 1.5 cycles/mm (approximately) due to the broader MTF of the smaller elements. Also, the MTF is truncated at the cut-off frequency of 2.5 cycles/mm as anticipated. The DQE is unchanged at low frequencies, and increased from approximately 0.2 to 0.4 at the cut-off frequency.

## 2.4 Conclusions

A method of improving the high-frequency DQE is proposed making use of sensor arrays with very small physical elements to synthesize larger image pixels. Called an “apodized-aperture pixel” (AAP) approach, will be most effective by combining high-resolution converters such as selenium with high-resolution sensors such as CMOS systems with 25  $\mu\text{m}$  or smaller sensor elements. A cascaded-systems analysis of signal and noise properties shows that:

- 1) The presampling MTF is improved due to the superior frequency response of the small sensor elements;
- 2) Use of a sinc-shaped kernel when synthesizing larger image pixels preserves the improved MTF and blocks frequencies above the image sampling cut-off frequency of  $f_c = 0.5/a$  for images with pixel size  $a$ . As a result, the presampling MTF does not extend beyond this frequency.
- 3) Noise aliasing is largely removed from the image although the Wiener NPS remains flat over all spatial frequencies.

- 4) Low-frequency DQE values are not affected by the AAP algorithm, however DQE values at the cut-off frequency are increased by a factor of up to 2.5x.
- 5) The AAP concept was validated experimentally on a CMOS/CsI-based detector with 0.05-mm elements by comparing 4x4 binning to simulate a 0.2-mm detector with using the AAP approach to synthesize images with the same pixel size. The high-frequency DQE was increased from 0.2 to 0.4.

## 2.5 References

1. E.J. Hall, "Radiobiology for the radiologist," 4th ed. 1994, Philadelphia: J.B. Lippincott. xii, 478 p.
2. E.J. Hall, D.J. Brenner, "Cancer risks from diagnostic radiology," Br J Radiol, 2008. **81**(965): p. 362-378.
3. A. Berrington de Gonzalez, S. Darby, "Risk of cancer from diagnostic X-rays: estimates for the UK and 14 other countries," Lancet, 2004. **363**(9406): p. 345-351.
4. "Medical imaging - The assessment of image quality - Int-Commiss-Radiat-Units-Measurements," Percep Mot Skills, 1996. **82**(3): p. 1391-1391.
5. H.H. Barrett, K. Meyers, "Image Science: Mathematical and Statistical Foundations," 2001: Wiley.
6. R. Shaw, "The equivalent quantum efficiency of the photographic process," J. Photogr. Sci, 1963. **11**(199-204).
7. J. Dainty, R. Shaw, "Image Science," Academic, New York, 1974. Ch. 2: p. 39-42.
8. R.M. Nishikawa, M.J. Yaffe, "Signal-to-Noise Properties of Mammographic Film Screen Systems," Med Phys, 1985. **12**(1): p. 32-39.
9. R.M. Nishikawa, M.J. Yaffe, "Effect of Various Noise Sources on the Detective Quantum Efficiency of Phosphor Screens," Med Phys, 1990. **17**(5): p. 887-893.
10. R.M. Nishikawa, M.J. Yaffe, "Model of the Spatial-Frequency-Dependent Detective Quantum Efficiency of Phosphor Screens," Med Phys, 1990. **17**(5): p. 894-904.
11. J. Tanguay, S. Yun, H.K. Kim, I.A. Cunningham, "Detective quantum efficiency of photon-counting x-ray detectors," Med Phys, 2015. **42**(1): p. 491-509.

12. I.A. Cunningham, R. Shaw, "Signal-to-noise optimization of medical imaging systems," J Opt Soc Am Opt Imag Sci Vis, 1999. **16**(3): p. 621-632.
13. I.A. Cunningham, J. Yao, V. Subotic, "Cascaded models and the DQE of flat-panel imagers: Noise aliasing, secondary quantum noise and reabsorption," Med Imag 2002: Phys Med Imag, 2002. **4682**: p. 61-72.
14. I.A. Cunningham, "Applied linear-systems theory," Handbook of medical imaging, 2000. **1**: p. 79-159.
15. G. Hajdok, J.J. Battista, I.A. Cunningham, "Fundamental x-ray interaction limits in diagnostic imaging detectors: Frequency-dependent Swank noise," Med Phys, 2008. **35**(7): p. 3194-3204.
16. S.N. Friedman, I.A. Cunningham, "A spatio-temporal detective quantum efficiency and its application to fluoroscopic systems," Med Phys, 2010. **37**(11): p. 6061-6069.
17. Yun, S., J. Tanguay, H.K. Kim, I.A. Cunningham, "Cascaded-systems analyses and the detective quantum efficiency of single-Z x-ray detectors including photoelectric, coherent and incoherent interactions," Med Phys, 2013. **40**(4).

## Chapter 3

### 3 Optimization

The AAP method introduces a process to create images with pixels that no longer correspond directly to physical detector-element measurements. Rather, image pixels are created from a two-dimensional convolution of detector data from very small detector elements. This process is represented both as a convolution in the spatial domain and as multiplication by the filter  $F(u)$  in the spatial-frequency domain as illustrated in Fig. 2-4. Two iterative approaches were used to determine an optimal filter shape that will maximize

the area under the DQE curve. Those two ways are shrinking and expanding algorithms of the Matlab AAP detector model simulation.

### 3.1 Methods

For the purpose of optimization, the Filter was represented as a 1024-element vector in the Fourier domain extending from  $u=-4u_c$  to  $u=4u_c$  where  $u_c=0.5/\varepsilon$  is the sampling cut-off frequency associated with the very small detector elements of width  $\varepsilon$ . The DQE was calculated using the CSA model up to the image cut-off frequency  $u_c=0.5/a$  where  $a$  is the image pixel spacing after implanting the AAP method. The shape of the filter vector was adjusted to maximize the area under the DQE curve.

In the first (shrinking) approach, the filter vector  $F$  was initially set to a value of one at all frequencies. The DQE was determined using the CSA model in Fig. 2-4 and the area under the DQE curve calculated. In the second iteration, the highest two non-zero frequency values in the vector  $F$  were set to zero and the DQE area recalculated. In this way, the filter was kept as a simple rectangle (low-pass filter) with a passband (rectangle half width) that was decreased with each iteration. This process was repeated until the DQE area stopped increasing to determine the maximum filter bandwidth that gives a maximal DQE area.

In the second (expanding) approach, the filter vector  $F$  was initially set to zeros in all elements except the single element corresponding to  $u=0$  where it was set to one. The DQE was determined using the CSA model in Fig. 2-4 and the area under the DQE curve calculated. In the second iteration the first element in  $F$  beside the  $u=0$  element on both positive and negative frequencies was increased from 0 to 0.1 and the DQE area recalculated. If the area increased from the previous iteration, those same elements in  $F$  were increased from 0.1 to 0.2. This process was repeated until the element of  $F$  reached a value of 1, when the next element in  $F$  on both positive and negative sides was increased. The iterations were continued until the DQE area stopped increasing to determine the lowest filter values and minimal filter bandwidth that gives a maximal DQE area.

## 3.2 Results

Results from the shrinking approach as shown in Fig. 3-1. The DQE area is shown as a function of iteration number. As the filter bandwidth was reduced with each iteration, the NPS bandwidth was reduced. As a result, the total aliased noise power in the image was decreased by decreasing aliased noise into the image frequencies below  $u_c=0.5/a$ . The filter also has an effect on the presampling MTF by zeroing the MTF at frequencies above the filter bandwidth. However, since it does not affect the presampling MTF at frequencies passed by the filter, only aliased noise power is affected by the decreasing filter width. The DQE and therefore DQE area were therefore increased with the first iterations.

The DQE area reached a maximum when the filter bandwidth equaled the image sampling cut-off frequency  $u_c=0.5/a$ . As the filter bandwidth was decreased further, both presampling MTF and NPS were truncated by the filter bandwidth. This did not affect DQE values passed by the filter, but it did reduce the DQE area.

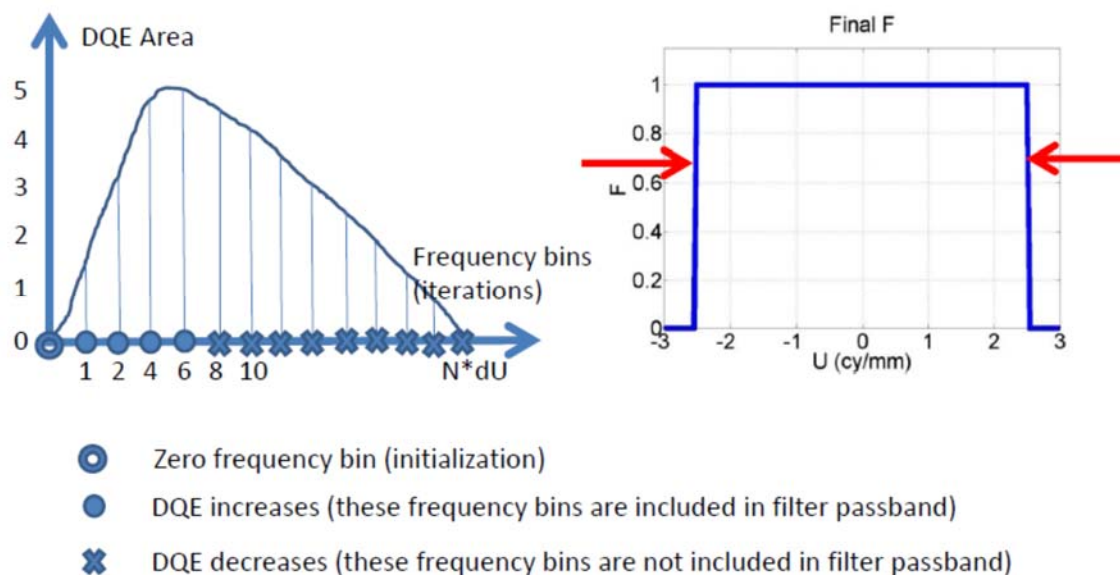


**Figure 3-1. Illustration of the shrinking mechanism of the AAP approach.**

Results from the expanding optimization are shown in Fig. 3-2. When the filter was initially very narrow, passing only the zero-frequency value, the DQE area was very small. As the filter bandwidth was increased by setting the first non-zero-frequency value in  $F$  to

0.1, there was a small increase in DQE area. As the filter vector values were increased from 0.1 to 1, there were no further increases in the DQE area until the next frequency value was increased from 0 to 0.1.

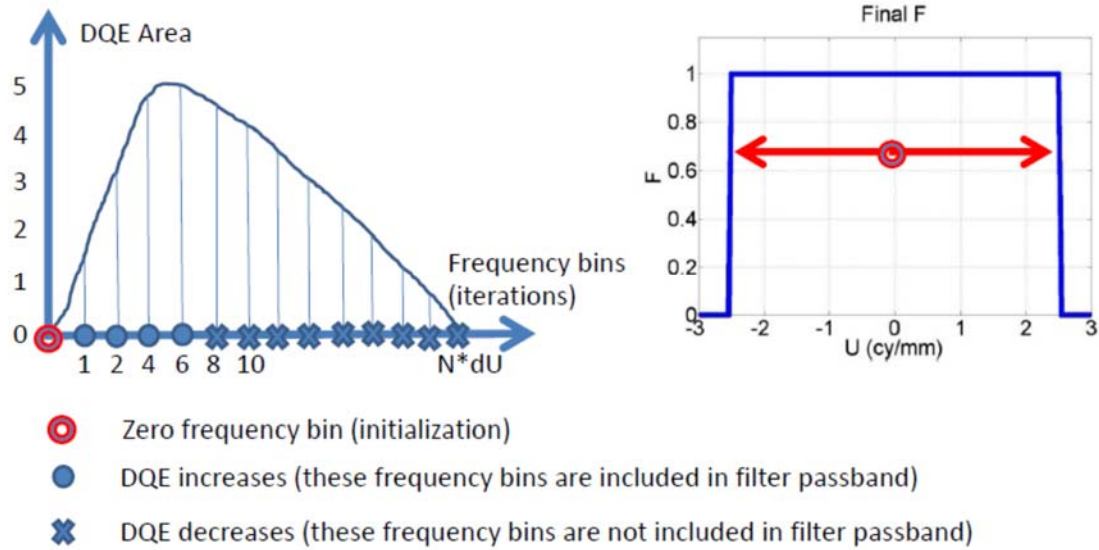


**Figure 3-2. Illustration of the expanding algorithm of AAP detector design.**

### 3.3 Conclusions

Both shrinking and expanding approaches to determining the optimal filter to use for the AAP method showed that the optimal filter width corresponded to the image sampling cut-off frequency of  $u_c = 0.5/a$  for image pixels with centre-to-centre spacings  $a$ . In addition, the expanding approach showed that the actual shape of the filter is not important as long as the filter contains non-zero element values up to the frequency  $u_c$ . This is seen by noting the filter shape will affect the system MTF as illustrated in Fig. 3-2, scaling the *MTF* by  $F(u)$  and the *NPS* by  $F^2(u)$  below  $u_c$ . As a consequence, the DQE is not affected by filter shape as long as the filter does not contain zero values for  $|u| < u_c$  and only zero values for  $|u| > u_c$ . The optimal filter shape can be any shape subject to this condition, within the assumptions used for the CSA model (no detector additive noise, ideal photon counting detector response with no energy dependence or x-ray scatter).

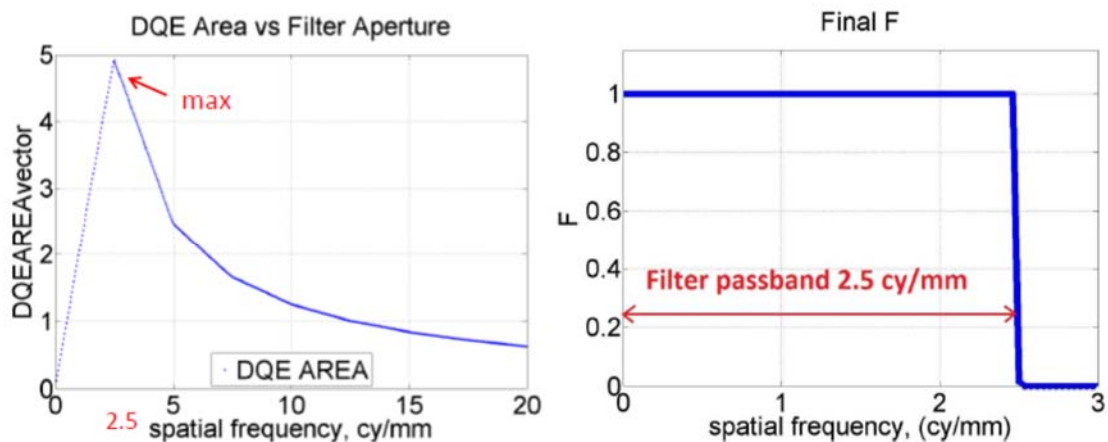


**Figure 3-3. MatLab simulation of an AAP filter optimization. Left plot: evaluation of the DQE area as an optimization criterion that determines the AAP filter aperture (right plot).**

## Chapter 4

### 4 Overview and Conclusions

#### 4.1 Limitations

The apodized-aperture pixel (AAP) design is proposed as a method of increasing the detective quantum efficiency (DQE) of x-ray detectors for medical imaging. The method requires the use of detectors with small physical sensor elements,  $\frac{1}{4}$  the size of the final image pixels or less, to synthesis final image pixels. It separates the pixel size from the detector sensor element size and improves the DQE by reducing noise aliasing and other benefits. The method could be implemented using a CMOS sensor coupled to a selenium converter layer.

The AAP method results in a DQE improvement by increasing the MTF and decreasing the NPS. The aperture MTF obtained using a detector with elements of width  $a$  is given by  $T_a(u) = |\text{sinc}(au)|$ . By using micro-elements of width  $e$ , the aperture MTF is increased to  $T_e(u) = |\text{sinc}(eu)|$ . Use of a sinc-shaped kernel to pass frequencies  $|u| < 0.5/a$  (the sampling cut-off frequency for pixels of size  $a$ ) when synthesizing larger image pixels preserves the improved aperture MTF and blocks frequencies above the cut-off frequency, corresponding to an increase in MTF by the factor  $M(u)$ , where:

$$M(u) = \begin{cases} \frac{\text{sinc}(eu)}{\text{sinc}(au)}, & |u| < u\epsilon/2 \\ 0, & |u| > u\epsilon/2 \end{cases}$$

As a result, while the presampling MTF of a conventional detector can extend to very high frequencies (potentially unlimited), the presampling MTF of the AAP detector is truncated to the Nyquist sampling cut-off frequency [1].

#### 4.2 Conclusions

Noise aliasing is largely removed from images although the Wiener NPS remains flat over all spatial frequencies in our simulations. Low-frequency DQE values are not affected by



the AAP algorithm, however DQE values at cut-off frequency are increased by a factor of up to 2.5x.

The AAP concept was validated experimentally on a CMOS/CsI-based detector with 0.05-mm elements by comparing 4x4 binning to simulate a 0.2-mm detector with using the AAP approach to synthesize images with the same pixel size. The measured DQE at high spatial frequency increased from 0.2 to 0.4, which provided experimental proof of concept. The AAP approach could be realized even more effectively with an amorphous selenium convert detector due to negligible scatter of charges liberated in the selenium compared to optical scatter of light in CsI.

The following points summarize the specific conclusions from this work.

1. The AAP method preserves the aperture MTF associated with the size of the physical sensor elements  $\epsilon$ , rather than the lesser aperture MTF associated with the size of the image pixels  $a$ .
2. The method reduces image noise by implementing an anti-aliasing filter to remove noise frequency components above the image cut-off frequency  $u_c=0.5/a$ .
3. It is determined the combination of improved MTF and reduced NPS can double the DQE at the cut-off frequency. For a selenium-based mammographic detector, this could increase the high-frequency DQE from 0.35 to 0.70.
4. Experimental validation on a CMOS/CsI prototype detector showed a doubling of the high-frequency DQE from 0.2 to 0.4 for physical sensors  $\epsilon=50\mu\text{m}$  and image pixels  $a=200\mu\text{m}$ .

An alternative to synthesizing image pixels of size  $a$  might be to retain the full resolution in images with pixels of size  $\epsilon$ . However, there are practical problems with this suggestion when applied to a busy radiology department. Images are typically acquired with approximately 2 bytes/pixel and 2k x 2k pixels/image. A typical image is therefore approximately 8 Mbytes/image. Increasing this to 8k x 8k pixels/image results in

128 Mbytes/image. This increase by a factor of 64x of image size would place a severe demand on departmental resources at a time when fiscal restraint is critical. For example, a busy department that performs 100,000 x-ray procedures per year might acquire 2000 images per day. These images must be transmitted from an acquisition workstation to an archival system and usually multiple review workstations. Transmitting each image a minimum of 3 times corresponds to transmitting  $2000 \times 3 \times 128 \text{ Mbytes/day} = 800 \text{ GBytes/day}$ . At a maximum achievable capacity of 10 Mbytes/sec for a modern 1 Gbit/sec network, this would saturate the network for 22 hours each day. Since images are normally acquired and reviewed only during working hours, this is not possible. Displaying images on 8k x 8k monitors is not practical for routine work. The AAP approach makes it possible to improve image quality without increasing patient exposures or placing prohibitive demands on institutional infrastructure.

### 4.3 Future work

As a future work the following directions could be considered:

- 1) Expand the theoretical CSA model to account for additive noise, quanta scattering and reabsorption in the conversion layer of the detector array;
- 2) Implement AAP detector in mammography at low energies (below 30 keV) to avoid scattering of characteristic radiation;
- 3) Implement AAP detector with direct detection x-ray detectors (a-Se).

Those directions could provide more efficient use of the AAP detector making its implementation much more beneficial for medical screening and therefore diagnostics.

### 4.4 References

1. P.C. Bunch, R. Shaw, R.L. Van Metter. "Signal-to-noise measurements for a screen-film system," App Opt Inst Med XII. 1984. Int Soc Opt Photon.

## Appendix A: Copyright approval

Permission to reprint SPIE article “Apodized-Aperture Pixel Design to Increase High-Frequency DQE and Reduce Noise Aliasing in X-Ray Detectors”, Elina Ismailova, Karim Karim and Ian A. Cunningham, Proc. SPIE Medical Imaging, The Physics of Medical Imaging, 9412-12 (2015) in chapter 2 of this thesis is provided below.

Dear Ms. Ismailova,

Thank you for seeking permission from SPIE to reprint material from our publications. As author, SPIE shares the copyright with you, so you retain the right to reproduce your paper in part or in whole.

Publisher's permission is hereby granted under the following conditions:

- (1) the material to be used has appeared in our publication without credit or acknowledgment to another source; and
- (2) you credit the original SPIE publication. Include the authors' names, title of paper, volume title, SPIE volume number, and year of publication in your credit statement.

Sincerely,

Nicole Harris

Administrative Editor, SPIE Publications

1000 20th St.

Bellingham, WA 98225

+1 360 685 5586 (office)

[nicoleh@spie.org](mailto:nicoleh@spie.org)

SPIE is the international society for optics and photonics. <http://SPIE.org>

## Curriculum Vitae

**Name:** Elina Ismailova

**Education** Kemerovo State University, Physics Department, Russia,  
Undergraduate studies with Honor, 2005 - 2008

Moscow Engineering Physics Institute, Department of  
Experimental Nuclear Physics, Russia, 2008 - 2011

The University of Western Ontario, Department of Medical  
Biophysics, MSc, London, Ontario, Canada, 2014-2015

**Related Work Experience** Teaching Assistant  
The University of Western Ontario  
2012-2013

Laboratory and Research Assistant  
High Energy Astrophysics Department, Moscow Space Research  
Institute of Russian Academy of Sciences,  
2010 – 2012

Laboratory Assistant,  
Moscow Engineering Physics Institute,  
2009 –2010

### Publications

1) Ismailova E., Grebenev S.A., “Discovery and follow-up investigation of transient X-ray sources IGR J17473-2721 and IGR J17419-2802 by INTEGRAL observatory data”, Letters to Astronomical Journal, (Russian), 03/2011

2) Ismailova E., Karim S. K., Cunningham I.A., “Apodized-Aperture Pixel Design to Increase High-Frequency DQE and Reduce Noise Aliasing in X-Ray Detectors”, Proc. SPIE Medical Imaging, Physics of Medical Imaging, 9412-12 (2015)

3) Nano T., Escartin T., Ismailova E., Karim K., Lindstrom J., Kim H.K., Cunningham I.A., “Apodized Aperture Pixel Design for Improved Detective Quantum Efficiency of X-Ray Detectors”, IEEE Transactions on Medical Imaging, submitted

### **Presentations**

1. 8th INTEGRAL Workshop “Restless gamma ray Universe”, Dublin, Ireland, Sept 2010, poster
2. “Discovery and follow-up investigation of transient x-ray sources IGR J17473-2721 and IGR J17419-2802 by INTEGRAL observatory data”, 18th Conference of Young Astronomers 2011, Kiev, Ukraine
3. “Apodized-aperture pixel design to increase high-frequency DQE and reduce noise aliasing in x-ray detectors”, Orlando FL, SPIE, Medical Imaging 2015
4. “Apodized-aperture pixel design to increase high-frequency DQE in x-ray detectors”, ImNO 2015, London ON
5. Apodized-aperture pixel design to increase high-frequency DQE and reduce noise aliasing in x-ray detectors”, World Congress on Medical Physics 2015, Toronto ON